MARS EXPLORATION ROVER (MER) PANORAMIC CAMERA (PANCAM) TWILIGHT IMAGE ANALYSIS FOR DETERMINATION OF PLANETARY BOUNDARY LAYER AND DUST PARTICLE SIZE PARAMETERS

A Thesis

by

STEPHANIE BETH GROUNDS

Submitted to the Office of Graduate Studies of
Texas A&M University
in partial fulfillment of the requirements for the degree of

MASTER OF SCIENCE

December 2010

Major Subject: Atmospheric Sciences

Mars Exploration Rover (MER) Panoramic Camera (Pancam) Twilight Image Analysis for Determination of Planetary Boundary Layer and Dust Particle Size Parameters

MARS EXPLORATION ROVER (MER) PANORAMIC CAMERA (PANCAM) TWILIGHT IMAGE ANALYSIS FOR DETERMINATION OF PLANETARY BOUNDARY LAYER AND DUST PARTICLE SIZE PARAMETERS

A Thesis

by

STEPHANIE BETH GROUNDS

Submitted to the Office of Graduate Studies of
Texas A&M University
in partial fulfillment of the requirements for the degree of

MASTER OF SCIENCE

Approved by:

Chair of Committee,	Mark Lemmon
Committee Members,	George Kattawar
	Gerald North
Head of Department,	Kenneth Bowman

December 2010

Major Subject: Atmospheric Sciences

ABSTRACT

Mars Exploration Rover (MER) Panoramic Camera (Pancam) Twilight Image Analysis for Determination of Planetary Boundary Layer and Dust Particle Size Parameters.

(December 2010)

Stephanie Beth Grounds, B.S., Angelo State University; M.S., University of Phoenix

Chair of Advisory Committee: Dr. Mark Lemmon

How the dust cycle works on Mars is a key atmospheric issue, as the dust cycle is arguably the dominant cycle in the current Martian climate. In addition, how much is known about the Martian planetary boundary layer is mostly determined from models with very little in-situ data from contemporaneous studies to validate such boundary layer characteristic assumptions, and the model studies have not been able to define a known height for a possible boundary layer on Mars using ground-based investigations prior to this research. The Mars Exploration Rovers (MERs), however, show promise in offering a unique chance to take surface-based measurements to offer support for dust and boundary layer measurements made from remote sensors. There are three main objectives of this study: to constrain the late-afternoon maximum height of the boundary layer for both MER sites, to constrain the mean particle size and variance of the size distribution in the atmosphere, and to use these results to demonstrate that sunset and twilight imaging is a useful survey of otherwise difficult-to-determine parameters that are needed in several tools for studying Mars' atmosphere.

A modeling approach using twilight-based Sun imaging by the MERs (Sol 1959 for Spirit and Sol 695 for Opportunity) is used to constrain boundary layer and dust particle size parameters. After determining which parameters control which observables, resulting elevations and azimuths are matched up to specific observations from the available MER datasets. A Monte Carlo code produces the model that is then compared to Sol data with plotting of resulting error. Results include PBL height and structure estimations and plots along with generalized particle size information for each MER site on the given Sol. Figures show comparisons of this study's particle size results with that of previous studies as well as maps of fit qualities for boundary layer parameters compared to a contemporaneous modeled scale height estimation. Results show promise for planning future MER-based campaigns and models.

DEDICATION

I dedicate this work to God and to my family, without whom I am nothing.

ACKNOWLEDGEMENTS

First of all, I would like to thank God for giving me the strength to complete this mission and for the joys in my life to keep me smiling. I owe Him my everything, and I am so happy to have Him in my life.

I would like to thank my committee chair Dr. Mark Lemmon for his help and guidance during the creation and execution of this project. I would also like to thank my committee members, Dr. George Kattawar and Dr. Gerald North, for their patience and help throughout the course of my research. It has been a bumpy road, but I couldn't have gotten here without all of you. I really appreciate all of your time and help.

I would like to thank NASA for providing the grant that helped fund me throughout my research. I would also like to thank Dr. Ken Bowman and Dr. Sara Brooks for funding me with teaching assistantships my first year here at Texas A&M.

I would like to thank the Department of Atmospheric Sciences as a whole. The professors were always ready to help at a moment's notice, and I feel like I have come away with a top-notch education and a knowledge base that I could have only dreamed of before. The Atmo staff is top-notch and always ready to help in any situation. Barbara, Christine, Carria, Tara, Stephanie, Chris, Neil, and Pat, thank you for everything you did to make my life easier. I couldn't have made it without your kindness and help.

I would also like to thank my parents, Beth and Steve, without whom absolutely none of this would be possible. I love you so much, and you are my steadfast reasons for

being. You never have given up on me or let me give up on myself, and for that I am truly blessed. I would also like to dedicate this to my family. To Granny, Pappy, PaBo, Papa Steve, and Prunellie – you may not be here in person, but your spirit has never left my side. I miss you and love you with all my heart. To MaBo – I am so proud to be your granddaughter, and I can't thank you enough for your encouragement and love. I love you. To Carly and D-Don – your support has never wavered, and I am so happily blessed to call you family. I love you both so very much. To Aunt Mona and Uncle Larry – you are adding a second Aggie to the list, but you have always had a crazy niece who loves you. To L.D. and Eric – your encouragement has always meant so much to me, and I love you both like the brothers I never had. To Daisy, Sam, and all of my babies – I love you and miss you so much. You keep my heart warm and full of love, always.

To all of my friends and Church back home, your support means the world to me. Thank you for always believing in me even when I didn't.

To Katie Connor – God bless you little one, and may He keep you safe and smiling in his arms. I send my love on the wings of an Angel.

I would like to thank my friends, who have helped me through from day one. I will never forget your kindnesses and support. Those of you who have been there from the beginning, I owe you the most thanks of all. Jen, Abby, Justin, Liz, Sean, Ellie, Christina, and Crystal, thank you for everything. I will never forget what you did for me, and I will always be in your debt.

Jennifer, thank you for always lending a shoulder to lean on and making me laugh when I wasn't sure I could go on. Who knew when I first met you outside the

O&M building that I had just met one of the best friends of my entire life. They say that best friends are forever, and I hope I still know you and can count you as a part of my life for at least that long.

Justin, we have had some amazing adventures and laughs together from the boot shop truck return to the e^{ghost} dilemma and chugga sewing machines. Thank you for never being afraid to tell me when I am being silly over something and for giving me the courage to be strong when I thought I couldn't succeed. You are a big part of me getting through these last few years, and I will never forget that.

Abigail, in the short time that I have known you, I have never gone a single day without smiling or laughing thanks to our little chats. I respect you so much for your wisdom and smart advice. You never let me forget that uniqueness is a special gift. Even though we often need a translator (gimmie cap and dressing anyone?), I cherish every single moment I have known you. Life is rarely a dream world, but you never let me forget that dreams are a never-ending part of happiness. Soul mates also come in the form of life-long best friends, and I thank God for putting you in my life just when I needed you most.

Damon and Desmond, you kept me smiling every time I thought I was ready to walk away from it all. Thanks to you two I am able and ready to fight through just about anything. You keep me fearless, and I adore you! *cue the crow and WW2010 patrol*

Mom and Dad, I just want to say thanks again. I know that sometimes it seemed like I was ready to give up and just walk away, but you never let me get past the first sentence of that speech. Any time I need any kind of help I know you will be there with

open arms and open hearts. People say you can't pick your parents. What they never finish saying is that God can pick them out for you, and He picked the very best he had ever seen for mine. I love you.

Last, but definitely not least, I want to be sure to thank this "rollercoaster called life" for putting wonderful people right where I needed them when I needed them most. You are all special and fabulous, and I could not have done this without all of you. Thank you with all of my heart.

TABLE OF CONTENTS

1. INTRODUCTION: THE IMPORTANCE OF MARTIAN DUST RESEARCH

Mars has frequently been the subject of mankind's wonder and imagination. From the "discovery" of Mars before recorded history while man looked up into the night sky to the multitude of Mars enthusiasts who search for new Rover images as soon as they are available, Mars has seemed to invoke more questions than science currently has answers for. One particular question that needs to be answered concerns the planet's boundary layer and associated dust structure. How much is known about the Martian planetary boundary layer is mostly determined from models with very little in-situ data from contemporaneous studies to validate such boundary layer characteristic assumptions, and the model studies have not been able to define a known height for a possible boundary layer on Mars using ground-based investigations prior to this research (Sorbjan, 2007a, 2007b; Taylor et al., 2007; Hinson et al., 2008; Sorbjan et al., 2009; Spiga and Forget, 2009; Spiga et al., 2010). The Mars Exploration Rovers (MERs), however, show promise in offering a unique chance to take surface-based measurements to offer support for dust and boundary layer measurements made from remote sensors (Lemmon et al., 2004a).

Mars has different atmospheric characteristics from those on Earth. For example, the solar constant for Mars is approximately 44% of the value for Earth (varying by approximately 20%), and the temperature ranges on Mars (- 125°C to +25°C) slightly

---

This thesis follows the style of the *Journal of Geophysical Research.*

overlap those on Earth (- 80°C to +50°C) (Larsen et al., 2002). A larger fraction of the solar radiation reaches the surface of Mars (up to 80%) as compared to what reaches the surface of Earth (up to 50%), and the near-surface air temperature is quite lower on Mars (- 50°C compared to 15°C on Earth) (Larsen et al., 2002). The Martian atmosphere is also composed mainly of carbon dioxide, and the surface pressure on Mars is less than one hundredth of that on Earth (Larsen et al., 2002). Due to a relatively high eccentricity in orbit, Mars also exhibits differing amounts of carbon dioxide condensation at the poles during the winters, which thereby causes a variation of air pressure during the Martian year (Larsen et al., 2002). Parameters controlling planetary boundary layer characteristics such as air pressure (1015 hPa on Earth and 6 – 7 hPa on Mars) and density cause subsequent differences in kinematic viscosity, heat capacity, and heat conductivity between the two planets (Larsen et al., 2002). Other parameters such as length of day and atmospheric scale heights are very similar between the two planets (Larsen et al., 2002). Table A1, adapted from Larsen et al., 2002, shows a set of parameters and the values for both Earth and Mars.

This study seeks to establish a means of using Mars Exploration Rover data to demonstrate that sunset and twilight imaging is a useful survey of otherwise difficult-to-determine parameters that are needed in several tools for studying Mars' atmosphere. This thesis will utilize a Monte Carlo-based model analysis of a set of sensitivity test-determined parameters and then apply data from sunset images taken by both rovers to determine boundary layer and general dust size parameters. This method will prove to be

an innovative use of Mars rover imaging datasets for both boundary layer and dust parameter applications.

1.1 Background and Previous Research

How the dust cycle works on Mars is a key atmospheric issue, as the dust cycle is arguably the dominant cycle in the current Martian climate (Kahn et al., 1992). One important aspect of this cycle is how the vertical dust distributions act as a tracer. Other issues lie with the lack of knowledge of Martian boundary layer characteristics and how the Martian boundary layer responds to the very different Martian conditions as compared to the relatively well-measured boundary layer on Earth. In order to understand the dust cycle itself, fundamental knowledge of the physical and mineralogical properties of Martian dust is necessary.

Remote sensing has long been the key source for most of the knowledge concerning Martian dust parameters and vertical distribution structure. Scientists have determined from prior measurements completed by remote sensing observations that the Martian dust is not spherical, but rather the dust is more likely an amorphous shape or even an aggregate shape of several particles (Pollack et al. 1979). Dust particle size and shape are related to residence time in the atmosphere, which in turn relates to how far dust can be transported during a lifting event. Dust can be transported via giant regional or planet-wide dust storms as well as via the movement of dust devils across the surface. The movement of dust in the Martian atmosphere is the main method through which resurfacing occurs today, and sedimentary structures literally come and go as the dust

entrainment and deposition change. Soil weathering is thought to be the main method that micron-sized dust particles become the key component of Martian aerosol (Korablev et al., 2005). The vertical distribution of these particles can then be used to determine boundary layer structure.

On Earth, the boundary layer represents an important concept for atmospheric modeling and measurement. The Earth's surface acts as the lowermost boundary condition for the atmosphere and interacts directly with the boundary layer itself, which in turn is greatly affected by this periphery (Wallace and Hobbs, 2006). There are several characteristics that define the PBL on Earth. The boundary layer can have heights from tens of meters to 4+ km above the surface, but the layer is normally ~1 -2 km in height (Wallace and Hobbs, 2006). Turbulence is found as superpositions of eddie swirls throughout the boundary layer, and it is this turbulence that allows for the dispersion of pollutants to the surface regions (Wallace and Hobbs, 2006). Within the boundary layer on Earth, heat and moisture are trapped and act as vital components necessary for convective clouds, and these clouds help drive weather patterns and can result in severe weather (Wallace and Hobbs, 2006). Changing weather patterns and a general diurnal cycle within the boundary layer also result in regional variations in boundary layer structure (Wallace and Hobbs, 2006).

Theoretically, the Martian boundary layer is a region in the lower atmosphere of Mars where vertical heat transport and dust are generally turbulence controlled, similar to the boundary layer on Earth (Zent et al., 1993). Based upon theory and modeled results, several assumptive statements about the boundary layer can be made. Turbulence

within the boundary layer can be mechanically or thermally driven, depending on the conditions (Zent et al., 1993). The boundary layer can vary from an average gas scale height of ~ 10.8 km in some regions during the day (Geirasch and Goody, 1968) to a few hundred meters above the Martian surface during the night (Haberle et al., 1993). The boundary layer is able to move a considerable atmospheric fraction on a daily basis, and therefore it is an important part of material exchange between the atmosphere and Martian surface, also similar to Earth (Zent et al., 1993). The convective boundary layer must exist on Mars without the deep convection associated with latent heat release from water vapor and cumulus clouds, however, as these atmospheric constituents do not play as large of a role on Mars as on Earth (Taylor et al., 2007). Boundary layers have been used in models for dust storm decay, and an influence on radiative heating due to a non-static dust distribution following a storm can be expected to affect the atmospheric structure (Taylor et al., 2007; Davy et al., 2009). According to temperature readings at a potential Phoenix Lander site near the North Pole during Northern Spring, a diurnal cycle of temperatures from -80°C to -10°C at the near-surface region implies a likelihood of a rather deep afternoon convective boundary layer (Taylor et al., 2007).

The Martian Planetary Boundary Layer (PBL) is not well documented (Sorbjan, 2007a, 2007b; Taylor et al., 2007; Hinson et al., 2008; Sorbjan et al., 2009; Spiga and Forget, 2009; Spiga et al., 2010). Previous research has shown that the boundary layer on Mars is difficult to describe either dynamically or structurally without measurements to validate model results. According to Martinez et al. (2009) there are three main categories of papers referring to Martian PBL studies: analytical 1-D simulations

(Gierasch and Goody 1968; Blumsack et al., 1973; Magalhaes and Gierasch 1982; Ye et al., 1990; Savijärvi 1991a, 1991b; Haberle et al., 1993; Savijärvi 1995; Savijärvi 1999; Savijärvi et al., 2004; Määttänen and Savijärvi 2004), 2-D models including surface layer similarity models (Savijärvi and Siili 1993; Siili et al., 1997; Odaka 2001), and 3-D models including large-eddy simulation (LES) models (Rafkin et al., 2001; Toigo and Richardson 2002). The results from these studies can generally be put into three main classes: vertical profiles (for temperature, radiative and turbulent heating rates, wind speed, and kinematic heat fluxes for specific times), diurnal in situ measurements used to test the model, and the ground energy balance (Martinez et al., 2009). These studies do not, however, define the Martian PBL characteristics in connection with ground truth observations from the MERs utilizing Pancam and a twilight imaging strategy.

The Martian PBL's meteorological parameters have rarely been determined via direct measurement (Smith et al., 2006), but certain in-situ measurements of the PBL have been previously made by Pathfinder and the Viking landers, allowing for a few PBL characteristics to be determined which can then be used in models (Hinson et al., 2008; Smith 2008; Spiga et al., 2010). During parachute descent, both Viking Landers were able to directly measure temperature in the Martian PBL (Seiff and Kirk, 1977; Smith et al., 2006). In addition, selected heights within a 1.5 meter layer above the surface of Mars were measured for parameters such as temperature, pressure, and wind velocity by the Viking and Pathfinder Landers (Hess et al., 1977; Sutton et al., 1978; Schofield et al, 1997; Smith et al., 2006). Occultation observations by Mariner 9 (Kliore et al., 1973), the Viking orbiters (Lindal et al., 1979), Mars Global Surveyor (Hinson et

al, 1999, 2001) and Mars Express (Hinson et al., 2008) only resulted in scattered remotely observed profiles which were not resolved enough vertically to provide distinct details about the boundary layer (Sorbjan et al., 2009). TES from Mars Global Surveyor retrieved temperature profiles from orbit (Christensen et al., 2004), but vertical resolution was not adequate to resolve the boundary layer characteristics (Sorbjan et al., 2009; Spiga et al., 2010).

Observations including temperature profiles and dust column optical depth have, however, been made using the MER Miniature Thermal Emission Spectrometer (Mini-TES) thermal infrared spectra (Smith et al., 2006). MER-based Mini-TES spectra have been used in the determination of generalized boundary layer parameters for Martian GCMs. Mini-TES spectra were collected in both the upward-looking and downward-looking geometries in the Smith et al. 2006 study. By using a timescale of a full Martian year, these spectra allowed for investigations into annual temperature variations as well as diurnal growth and decay of a highly superadiabatic layer found near the surface (Smith et al., 2006). Mini-TES observations were used to observe general timescales, duration times, and overall intensities of multiple local- and regional-scale dust storms, and upward-looking Mini-TES research can also be used to provide a "snapshot" of the convective and turbulent characteristics of temperature perturbations within the PBL (Smith et al., 2006). Turbulence is a possible factor for a higher PBL than assumed by the Mini-TES and other models as this would allow for better mixing during the highly convective daytime periods only to have that convection wane as sunset approaches. Mini-TES observations for the MERs were also made for the same seasonal time period

as radio occultation data from Mars Express, but the results when compared to the occultation data were inconclusive due to a lack of collocation and local time measurements (Hinson et al., 2008). Vertical potential temperature profiles were determined by the Spirit MER in 2004-2005 during the first 702 Sols in a study by Sorbjan et al. (2009). These temperature profiles in the 2009 Sorbjan et al. model were determined using mini-TES measurements up to a 2 km point above the surface and were used to reconstruct both a diurnal and seasonal structure of the lower 2km portion of the Martian CBL as well as evaluate the boundary layer depth structure. Mini-TES observations show possibilities when determining parameters which can be used to resolve boundary layer characteristics, but these Mini-TES measurements do not offer the spatial or temporal scale needed to make these determinations efficiently for the entire height of the PBL. A soil-atmosphere column model by Savijärvi and Kauhanen (2008) was compared to Mini-TES observations from the rovers, and while it was found that surface temperature profiles were well simulated overall by the model, an overestimation of the temperatures during the perihelion/summer period was possibly due to mishandling of dust within the model itself. Dust accumulation on the rover optics, calibration drifting during the relatively long rover lifetimes, and sensitivity to pressures and initial temperature profiles may have caused skewed results within the model (Smith et al., 2006; Savijärvi and Kauhanen 2008). Both the Savijärvi and Kauhanen (2008) model and the MER direct Mini-TES observations showed a very defined warming and cooling daily behavior with a robustly superadiabatic surface layer during the morning hours (due to thermal emission from solar heating of the ground

being partially absorbed by relatively cooler dust and CO_2 aloft) and a convective boundary layer (CBL) being created by the convection that carries this absorbed heat upwards. The surface layer is then cooled according to Savijärvi and Kauhanen (2008), and during the evening hours, a robust surface inversion results through radiative cooling. Both Mars Odyssey THEMIS and Mars Global Surveyor TES was able to observe the December 2003 dust storm prior to the rover landings, and later observations show differences between dust optical depth between retrieved values from orbit and those found by Mini-TES (orbital values tend to be systematically lower than Mini-TES values by ~ 10 – 50%) with these differences in dust optical depth possibly being due to the fact that a well-mixed profile is assumed for Mini-TES observations (Smith et al., 2006).

Large-eddy simulations (LES) have been studied with respect to the Martian PBL that focus on arid, shallow, daylight-based convection which in turn represents a quasi-steady Martian atmosphere, and as Martian air is thinner, the PBL has a strong response to turbulent fluxes with pronounced Martian turbulence due to a smaller gravitational effect and lower air density (Sorbjan, 2007a, 2007b). Comparisons between RO retrievals and LES data were used by Spiga and Forget (2009) and Spiga et al. (2010) to quantitatively compare LES predictions with measured parameters. Mars Express RO temperature profiles and simulations using large-eddy approaches from the Martian mesoscale model were used to determine the structure of the Mars convective boundary layer (CBL) (Spiga and Forget 2009; Spiga et al., 2010). Laboratoire de Météorologie Dynamique (LMD) schema for soil, surface layer, and radiative transfer Mars

parameters were combined with the Weather Research and Forecast non-hydrostatic model core as the main focus for the 2010 Spiga et al. study. A positive correlation was also found between planetary topography and upper height limit for the boundary layer (Spiga et al., 2010). This correlation further emphasizes a need for collocation of study areas to be used in study comparisons. In a two-part study by Sorbjan (2007a, 2007b), it was found that by using LES the simulated boundary layer was found to have a three-layer structure, but observations were not available to validate this boundary layer structure. In a study by Taylor et al. (2007) a one-dimensional (horizontally homogeneous) unsteady eddy diffusion model was studied with the intent to characterize dust particle size and height distributions in the Martian PBL. Measurements from the Phoenix Lander using LIDAR backscatter to determine Martian PBL layering and depth characteristics were to be used to validate this study. The Taylor et al. (2007) model was intended to examine likely circumstances for the dust size distribution in the lower Martian atmosphere, and the modeled dust was assumed to either be advected from an outlying source or dust stemming from a local source. In the advection case, the initial dust size distribution within the atmosphere followed a modified gamma distribution. Large dust particles deposit rapidly from the atmosphere while the smaller dust particles are well mixed to the upper limit of the afternoon Martian PBL with much slower deposition rates than the larger particles (generalized settling velocities of ~ 100m/Sol) (Taylor et al., 2007). These small particles, if mixed to heights ~10km, can be advected through long distances even in the absence of sustained turbulence to continue the particle suspension, which is important when trying to decide where dust particles

originated (Taylor et al., 2007). In the local sourcing case for the Taylor et al. 2007 model, surface dust source parameterization was utilized while still maintaining a modified gamma distribution for the initial concentrations. Model results showed that small particles exhibited rapid mixing within the Martian PBL while the larger particles ($r > 10\mu m$) remained concentrated along the ground surface while exhibiting a more intense diurnal cycle. Small particles with an $r_{eff} = 1.6\mu m$ show variations in both the mean and variance of the area-weighted radius in the Taylor et al. (2007) model while still being well represented by a modified gamma distribution, but larger particles at the surface ($r = 50\mu m$) are not well represented by the modified gamma distribution. A study by Davy et al. (2010) utilized a coupled boundary layer – Aeolian dust model to determine how emission, scattering, and absorption by dust particles would affect the boundary layer and by doing so, affect the dust allocation within the atmosphere.

In other studies the modeled PBL is found to have a range of varying heights from ~ 4 – 10 km using varying techniques. Hinson et al. (2004, 2008) used a May – August 2004 time period with radio occultation (RO) experiments from Mars Express which included a discrete and well-mixed convective boundary layer (CBL) showing differences in depth ranging from ~8 – 10 km over higher elevations and ~ 4 – 6 km over lower surface elevations due to a larger impact of solar ground heating where surface pressure and atmospheric density are nominal over higher elevations. Properties from Tomasko et al. (1999) were used for both "*a*" (1.6μm) and "*b*" (0.2μm) in the initial dust size distribution in a study by Davy et al., (2010), and the boundary levels in this study varied from 6.5km to 9km. In a study by Sorbjan et al. (2009) the study elevation angle

was limited to > 20° above the horizon to limit uncertainties due to MER potential temperature profile sensitivities to elevation angle, and the overall height of the boundary layer was determined to be ~ 1- 2 km/hr from 9:00 to 14:00 Local True Solar Time (LTST) using the temperature profiles from the mini-TES observations. Modeled boundary layer heights range from around 3 km in late afternoon to ~ 1 km after sundown in the Taylor et al., (2007) model, but drawbacks include that a PBL dynamics model was used separately from the dust models, spherical dust particles are assumed, no observations are available to compare to/validate the model data, and that set boundaries of 1km and 10km for the upper and lower boundary layer levels were used.

A PBL model was coupled with the Taylor et al. (2007) model to determine whether or not Phoenix LIDAR would be useable for further study of the boundary layer depth as determined using dust distribution (Davy et al., 2010). Model runs within the Davy et al. (2010) study were again run for two scenarios: one with dust advection from a remote source and one with local dust origination lifted from the surface of Mars by surface wind stress. Whiteway et al. (2009) describe a Phoenix Lander ice-cloud detecting mission (utilizing a light detection and ranging (LIDAR) instrument and measuring dust in the atmosphere) that found a well-mixed PBL on Mars up to a height of around 4 km during the summer turbulence and convection. LIDAR measurements from the Phoenix Mars mission were interpreted in a study by Daerden et al. (2010) utilizing a PBL model coupled with a microphysical model for dust and ice clouds. The Daerden et al., (2010) model predicted a depth of 4km for the PBL, which was similar to the daytime dust observations from the Phoenix LIDAR. Large-eddy simulations

quantitatively reproduced regional disparity as validated by the Spiga et al., (2010) model, and boundary layer depths were found to approach 9 km.

Twilight studies have been completed using scale height models. Twilight is defined as the time period when the sun falls below the local horizon, thus resulting in a direct solar illumination of the overhead sky (Kahn and Goody, 1981). As the sun sets, it shines on progressively higher and higher portions of the atmosphere due to geometry, therefore allowing for the probing of different sections of the atmosphere depending on timing of the observations. Viking Lander twilight observations were used to probe into the atmosphere to determine the vertical distribution of Martian scattering properties (Kahn and Goody, 1981). The resulting modeled conclusions found the data to be consistent with a dust scale height of 10 km, and a general conclusion of a well-mixed atmosphere with consistent lower level dust was made from this study (Kahn and Goody, 1981). Due to a lack of useable data to add other parameters to the study, no boundary layer information resulted. Lemmon et al. also used a scale height model to determine the dust airmass from low-elevation Sun images. Airmass was modeled as if it were controlled by scale height as a single-parameter model (Lemmon et al., manuscript in preparation, 2010).

1.2 Study Justification and Objectives

This study will be of specific importance to the creation of global climate models (GCMs) for use with Mars-related data as Martian GCMs can be useful tools that allow scientists to better understand the Martian atmosphere. GCM builders are in need of

observational constraints for their models, and an important part of building Martian GCMs is to determine the general structure of the boundary layer. Prior to the MER mission, information about the vertical structure well into the Martian boundary layer was not readily available (Sorbjan et al., 2009). Current boundary layer estimates for models are generally based upon assumption as there is very little measured dust-related data available with which to determine the actual heights and parameters for the boundary layer on Mars (Sorbjan, 2007a, 2007b; Taylor et al., 2007; Hinson et al., 2008; Sorbjan et al., 2009; Spiga and Forget, 2009; Spiga et al., 2010). It is evident that the theoretical height of the boundary layer varies depending on the time period studied. As there have been relatively few direct measurements of parameters for the PBL on Mars, retrieved temperature profiles allow for a generalized parameterization for boundary layer schemes utilized by global and mesoscale Martian atmospheric models (Smith et al., 2006).

Another difficult issue to work with in a Martian GCM is the uncertainty of the dust as the dust on Mars is a known driver for the deposition of energy throughout the atmosphere (Pollack et al. 1979, 1995; Tomasko et al. 1999; Lemmon et al. 2004; Wolff et al. 2006). Martian dust acts as an all around climate manipulator due to its sheer abundance on the surface and large quantities suspended in the air. Dust particles also play a critical role in the Martian climate (through an extended time-scale global circulation effect) and the global radiation and energy budget (Markiewicz et al., 1999). In addition, the absorption of solar radiation by the dust particles in the Martian atmosphere affects the temperature structure and atmospheric dynamical forcing

(Tomasko et al., 1999). The airborne dust absorbs sunlight particularly well in the range of 400nm to 600 nm and thermal radiation near 9μm (Lemmon et al., 2004a). In general, the heating of the atmosphere via absorbed infrared and solar radiation mainly comes from absorption by the suspended atmospheric dust particle instead of any of the other less abundant atmospheric constituents (Gierasch and Goody, 1972; Pollack et al., 1979; Haberle et al., 1982).

Previous dust-related studies have been done using both cross-sectional and volume-based models and measurements (Pollack et al. 1979, 1995; Tomasko et al. 1999; Lemmon et al. 2004; Wolff et al. 2006). Martian dust is not easily monitored from space through visible imaging due to the similarity in characteristics to the loose dust and mineralogical materials upon the surface of the planet, but newer technology in limb scanners and IR spectral instruments is attempting to solve this issue (Kahn et al., 1992; Smith and Lemmon, 1999; Vincendon et al., 2008a, 2008b). Airborne dust on Mars has related radiative properties (including single scattering albedo (ssa) and the asymmetry parameter (g)) that depend mainly upon dust particle size, shape, and composition (Pollack et al., 1995). Observations and measurements derive that the average effective particle radii for Martian dust particles are in the range from 1.5 to 1.7 μm (Tomasko et al., 1999; Pollack et al., 1995; Wolff and Clancy, 2003; Clancy et al., 2003, Lemmon et al., 2004a; Wolff et al., 2006). Earlier observations using Mariner 9 data resulted in a size range of the dust particles of 2.5 to 10μm, and during the peak of the 2001 Martian dust storm, TES-derived effective particle radii for the dust particles were found to be in a range of 1.0 to 2.5μm (Hartmann and Price, 1974; Conrath 1975; Wolff and Clancy,

2003; Clancy et al., 2003). Particle effective radii ranges are different according to measurement type, model used (if any), and measurement method. With the exception of the Wolff et al., 2006 infrared study, these measurements have been done at different times than the study presented in this thesis, which makes direct comparisons between studies difficult due to the inherent variability of dust particle population and characteristics with time.

Another way that dust-related measurements are important to Mars research is that they will aid in the facilitation of the success of the first manned mission to Mars. The presence of dust is a known major hazard for missions to Mars, both manned and robotic (Sharma et al., 2008). The hazards are numerous and range from the accumulation of dust upon critical solar panels, various seals, photovoltaic cell surfaces, and instrumentation mechanical and optical surfaces to health hazards to flight crews and astronauts (Sharma et al., 2008). In addition, the electrostatic properties of the charged dust particles can mean disaster via critical component failure and related injury to the crew (Beaty et al., 2005). It is vitally important to be able to approximate the dust that will be found on the Martian surface in order to prepare for a manned mission to Mars. Dust properties such as size are important to sending a manned mission to Mars because the potential harm to humans is directly related to both the amount of dust in the small end of the size distribution and its mineralogy. Spacecraft, crew suits, living quarters, medical treatment supplies – all of these things will have to be able to take on the rigorous daily life on a planet comprised mostly of dust. Plans need to be made now to make dust-resistance a certainty prior to sending the first man to Mars.

There are three main objectives of this study: to constrain the late-afternoon maximum height of the boundary layer for both MER sites, to constrain the mean particle size and variance of the size distribution in the atmosphere, and use these results to demonstrate that sunset and twilight imaging is a useful survey of otherwise difficult-to-determine parameters that are needed in several tools for studying Mars' atmosphere.

2. OBSERVATIONS

The Mars Exploration Rovers (MERs) began their traverse across the Martian surface on 4 January 2004 [Spirit, landing at Gusev crater – 14.75°S, 175.48°E] and 25 January 2004 [Opportunity, landing at Meridiani Planum – 1.95°S, 354.47°E] (Lemmon et al., 2004a). The rovers Panoramic Camera (Pancam) is comprised of a pair of stereoscopic multispectral cameras that are mast-mounted 1.5m above the Martian surface and have separate sets of eight-position filter wheels for each stereoscopic "eye" (Bell et al., 2003). Pancam offers multi-spectral observations via these filters (denoted as L1-L8 and R1-R8, L and R are notations for left and right) (Lemmon et al., 2004a). In addition, Pancam is both calibrated and designed to be able to function at varying temperatures on the Martian surface (-55°C to +5°C) while also allowing for sun-finding to aid rover navigation, digital modeling of Martian surface terrain, high-resolution imaging for sampling in an in-situ environment, and general mission support (Bell et al., 2003). Pancam acts as a multi-function camera – acting as a multi-spectral general science imager as well as the main camera for imaging the sun (Bell et al., 2003). Pancam images taken horizontally of the low-positioned sun as it traverses the sky and vertically based images of the sun at the highest "noon" point in the sky can both help determine various dust properties such as single scattering albedo (Pollack et al., 1995; Tomasko et al., 1999; Markiewicz et al., 1999). The filters are generally used for either

geological imaging or solar imaging, and the redundant wavelength filters for both left and right Pancams are used for both stereo two-color imaging and failure redundancy measures (Bell et al., 2003). There is instrumental scattered light, but the scattered light from the sky is three orders of magnitude larger, so the instrumental scattered light in this study is ignored.

Solar longitude (notated by L_s) is defined as 0 and 360 at northern spring Martian equinox and at approximately 90 at northern summer solstice. Spirit Sol 1959 (with solar elevation 1.1° and visible optical depth 0.49) and Opportunity Sol 695 (solar elevation 0.7° and visible optical depth 0.77) are the individual Sols used for the analysis. Both are within dust storm season, which is roughly during aphelion (L_s = 150) to the end of southern summer (L_s = 360, or 0). Martian dust storms are known to be particularly active during L_s = 220 through L_s = 330. Figure B1 shows optical depth for the MERs with data for Opportunity Sol 695 and Spirit Sol 1959 shown as black stars (Lemmon et al., 2004a; Lemmon et al., manuscript in preparation, 2010).

The data considered in this study consists of sky images near sunset, using the Pancam violet (L7) filter. Figure B2 shows pseudo-color sunset images from Spirit Sol 1959. The 15 images were taken from rover sequence AP2678, during which the Sun moved from 5.7° elevation to 1.1° elevation. The pseudo-color is used to show the large dynamic range and to enhance intensity. The brightness fades with distance from the Sun (controlled by narrowness of the single-scattering peak) and increases with elevation near the Sun (extinction and scattering controlled by airmass). The brightness also fades as the Sun sets (extinction controlled by airmass). Figure B3 shows sunset images in

pseudo-color from Opportunity Sol 659. The nine images were taken from rover sequence BP2662, during which the Sun moved from 2.0° elevation to 0.7° elevation.

3. METHODS

In this section the general processes behind the model and code are discussed. After determining which parameters control which observables (parameters and descriptions are found in Table A2), the resulting elevations and azimuths can then be matched up to specific observations from the available MER datasets. A Monte Carlo code produces the model that is then compared to Sol data with plotting of resulting error. Results include PBL height and structure estimations along with generalized particle size information for each MER site on the given Sol. In the single scattering section, considerations for the modeling process include assumptions, simplifications, and parameter information. The multiple scattering section includes considerations include information about Monte Carlo and backward Monte Carlo techniques and how they are applied to the model. Finally, a section describing the model implementation and data analysis steps through the model process in detail, including how boundary level dependence was determined from a preliminary one-layer model, how sensitivity tests were run to decrease the number of free parameters, and how a grid system was devised for image analysis.

3.1 Single Scattering Considerations

Mie scattering for dust particle sizes found on Mars predicts strong and high frequency oscillations. These oscillations are not observed, however, and this has resulted in modeling for scattering by irregular dust particles on Mars by lending

credence to the assumption that the dust particles are not spherical (Pollack et al., 1979; Pollack et al., 1995; Tomasko et al., 1999; Lemmon et al., 2004a). From Viking measurements to Pathfinder measurements, a parameterization of scattering by irregular particles has been utilized (Pollack et al., 1995; Tomasko et al., 1999). This model also makes the irregular particle assumption and uses the irregular particle parameterization described by such studies, which thereby introduces mathematical complications. While the radius alone adequately constrains the particle size for a sphere, for an irregular particle the dimensions needed for constraint on particle shape and size can be infinite due to the inhomogeneity of the particles themselves. To simplify the particle constraints, this study uses effective particle radius (a) and particle size distribution variance (b) parameters to determine the dust shape and size distribution. If the dust particles were a different shape (cubic or oblate for example), then another approach to determine the shape would be needed. Mars dust does not have regularity in dust shape, so a simplification of shape parameters must be assumed for simplicity of the model where the physics cannot easily be done.

A single scattering approach is utilized that is similar to the treatment used for single scattering by irregular particles by Tomasko et al., 1999, which in turn is adapted from a method previously used by Pollack and Cuzzi 1980. Scattering by particles below a critical size threshold are estimated using Mie scattering while larger particles are approximated by a sum of light that goes around a dust particle via diffraction, light that is bounced off the surface of the particle via external reflection, and a parameterized approximation for light transmitted internally by the particle (Pollack and Cuzzi, 1980;

Tomasko et al., 1999). Less than 10° from the sun diffraction dominates, and farther away from the sun transmission and reflectance dominate. If the reflection and transmission values are altered, then the phase function away from the sun itself is also altered, but the doubling of the light itself at this point will have a small effect on what is seen near the sun.

The model works so that if the imaginary index of refraction is changed, less light is transmitted, and the single scattering albedo is smaller while the shape of the phase function curve will remain the same. This is not necessarily realistic in nature, but this is an assumption made for the model again for simplicity. Any viewing angle below 15° above the horizon requires that a spherical shell atmosphere approach be used instead of a plane-parallel approach, and this study is looking at the sky at between 5° and 8° above the horizon. There is no need to perform Rayleigh scattering based on molecular scattering with CO_2 because the Martian atmosphere is only 7/10 of a percent as thick as Earth's atmosphere, and Rayleigh scattering has a very small effect in this case, even in the blue wavelength portion. Polarization is also ignored due to the fact that polarization of the dust on Mars is small and is not well known.

Single-scattering parameters include wavelength ($\lambda = 0.443$ μm) from the instrument description (Bell et al. 2004a, 2004b), n_r (1.5), from Tomasko et al. (1999), *G (115)*, θ_{min} (138), n_i (0.0101), from Johnson et al. (2003), optical depth ($\tau = 0.77$ for Opportunity site and 0.49 for Spirit site) from rover solar imaging (Lemmon, 2004b), and the size distribution mean and variance (*a*, *b*), tested in the models described below. Single scattering is made up of Mie scattering for the small particle part of the size

distribution and parameterized scattering for large particles (X> 5), with typical components shown in Figure B4. The parameterization includes diffraction, modeled as diffraction around a disk, for each size in the distribution, and prescribed reflection and internal transmission. Internal transmission is assumed to have a quadratic shape in log space specified by the angle of the minimum, θ_{min}, and *G,* the slope of the log of the phase function at angle 0 (Pollack and Cuzzi, 1980; Showalter et al., 1992). The phase function is then normalized, so the third constraint is arbitrary. Tomasko et al. (1999) showed that such a model is effective at numerically representing laboratory results for scattering by irregular particles. The model is not very sensitive to n_i (imaginary index of refraction), *G*, and θ_{min} when looking at a phase function not far from the sun (low sensitivity to mid- or large-angle scattering), so these values are modified from Johnson et al., 2003 and Tomasko et al., 1999.

The violet L7 filter is the most diagnostic of the filter set due to a shorter wavelength and narrower forward scattering profile, and it is the filter used for the analysis. As the study looks at the forward scattered light immediately near the sun, this is an important aspect to allow for the most diagnostic approach while shortening overall model run time by limiting filters for the runs. When the sun is low, the light has been scattered multiple times with each scattering event widening the photon distribution around the sky. By using a filter with a narrow forward scattering profile, the data is smoothed to a lesser degree than when using a wider photon distribution by keeping the photons in a relatively straight path between the camera and the sun. Essentially the photons have a better concentration which aids the model by keeping other noise out of

the runs. This is in addition to the physically shorter run time when using one filter rather than a combination of two or more filters.

3.2 Multiple Scattering Considerations

A Monte Carlo technique was chosen for this study because of the geometry of the viewing angle for the MER Pancam. The images under consideration show the sky near the Sun, at elevations of a few degrees. Under these conditions, plane-parallel assumptions break down: the airmass (ratio of slant path optical depth to normal optical depth) approaches infinity for a plane-parallel atmosphere at sunset, but is limited to around 20 for the Martian atmospheric scale height (about 11 km) and radius (about 3394 km). A Monte Carlo approach allows for the specification of arbitrary spherical geometry. The spherical-shell atmosphere is divided into multiple concentric spherical-shell layers, thereby allowing the application of different scattering and absorption coefficients and aerosol phase matrices in each layer that can be varied with altitude to allow for studies of the sky at twilight (Collins et al., 1972).

The Monte Carlo method is a method that uses statistical integration. When using a Monte Carlo method, the geometry is important, but the method of determining the phase function is not. Monte Carlo methods are the answer to the statistical integration versus time issue. Using classical integration, an area under a curve is subdivided and the point is counted as either in or out of a specific subdivision. Because the subdivision is not infinitely small, this is still only an approximation, albeit a close one. Adding in extra dimensions due to the fact that scattering is infinitely dimensional is an additional

numerical challenge. Monte Carlo allows for the random assessment of whether or not the photon is within the constrained area. Most points will miss the area, so the more constrained the area can be while still containing all possible solutions, the better. The error is roughly the square root of the number of points that fall on the curve. 1000 points in the area and 100 on the curve means a 10% error. With Monte Carlo constraints, however, the same 10% error can be achieved with 150 points for example due to the fact that the possible area for the point to fall on is as close to the curve as possible.

A backward Monte Carlo method is used in this case because it is the same general effect as constraining the photons, and the algorithm in this study is based on Collins et al., 1972. Half of Mars can see the sun at any given time, but only a small portion of Mars can see Pancam. The procedure for backward Monte Carlo is the same as time reversal (instead of simply exchanging the source and detector positions) (Adams and Kattawar, 1978). Instead of following every photon from the sun regardless of where it hits on Mars, a backward Monte Carlo method starts at the detected photon and reverses the path in time to see how much light could have hit that dust particle and scattered to reach the detector. The code takes advantage of the ease of computing single scattered light and computes it with a Newton's method integration. The code assigns a weight to the photon, and a photon has a weight of one when it starts. As an absorption event happens, a weight fraction is taken away from the photon. Every point between the camera and the sun is a possible stopping point at which point the photon will no longer be counted. Some fraction of the photons leaving the camera will leave the atmosphere,

and these photons are not followed while interaction with the ground (which is described as a Lambertian surface in this case) can mean absorption or another scattering event (Collins et al., 1972). A very small optical depth is integrated ahead of the photon, and this volume is viewed (along with the sun and the dust between the sun and the viewed volume). How much non-scattered light gets to the sun from the camera path is of importance, and the angle between where the sun is located and where the model is looking (along with the phase function) means that the probability is known as to whether or not the photon is scattered in a particular direction. If single scattered light is being viewed, then the integral is computed by stepping along an optical depth all the way out of the atmosphere. Using double scattered light increases the integration parameters from one to four. To do this, the integral is first computed through a single scattered path, and then the integral is computed over the distance that the photon is scattered, what the scattering angle value is, and the optical depth to the next scattering event. The code follows the photon until there is only 10^{-6} of it remaining and then it abandons it.

3.3 Model Implementation and Data Analysis

The structural model used is shown schematically in Figure B5. The atmosphere is considered to have two vertical regions. The first is from the surface to the top of the boundary layer, and is characterized by a dust size distribution (a, b), scale height (which is set to 11.5 km, the scale height for temperatures near sunset at 2 km elevation from Smith et al. 2006), and the altitude of the top of the boundary layer, Z_{lay}. The second

region is from the top of the boundary layer to the top of atmosphere, and is characterized by an arbitrary scale height, generally less than the mean atmospheric scale height of 11 km, and the same size distribution as in the boundary layer. The latter assumption is arbitrary and not likely to be strictly correct, but the models are not sensitive enough to be given too large a number of size distribution parameters. Finally, a discontinuity in dust density is assumed at the top of the boundary layer, expressed as $delta = N_{free}/N_{boundary}$. Using specific parameter values for *delta*, Z_{lay}, and scale heights with an arbitrary bottom-of-atmosphere dust density, the optical depth profile is calculated and normalized to the observed normal optical depth, allowing optical depth to be partitioned between the layers. Table A3 shows parameter ranges that were investigated.

The randomization of the varied parameters was determined in order to cover a wide range of 5-dimensional parameter space, and the parameters varied included *a* and *b* (size parameters), *delta* (the size of the discontinuity in the boundary level), *zlay* (the height of the lower layer), and *Hfree* (the height of the upper layer). In order to limit the number of parameters that required variation for the new multi-layer model, a sensitivity test was run. Characteristics of each layer include physical thickness, an extinction optical depth, and a scale height which describes the exponential variation with varying altitude within the layer itself. The combined layers are also characterized by a single phase function and single scattering albedo. After the parameter variations were completed, it was found that the model was most sensitive to phase function type, and

therefore particle size. In addition, reasonable layer structure changes also produced a significant impact on the model.

As optical depths are relatively static during the chosen Sols and other parameters are varying, the model's usefulness is tested by using the two sites with different optical depths ($\tau = 0.49$ for the Spirit Sol and $\tau = 0.77$ for the Opportunity Sol). Images are taken using the L7 filter and are rotated to level the true horizon. A boundary layer scale height was assumed to be the atmospheric gas scale height calculated for a 2-km temperature at 1800 LTST (Smith et al., 2006). The free atmosphere scale height was assumed to be the gas scale height calculated for 10° below that of Mars' equilibrium temperature, and airmass was then calculated for a range of the two scale height parameters assuming a solar elevation of 3°. An azimuth (± 1°, 2°, 3°, … from the sun) and elevation (+1, 3, 5, …) grid is used for modeling, as shown in Figure B6. The sampling for elevation is different than that of azimuth because it takes longer for Pancam to perform an extra elevation measurement vs. an extra azimuth measurement. Intensity was extracted from the images at each azimuth and elevation of the model grid and was interpolated to the solar elevations of 1° and 2° from the grid for Opportunity and 1°, 2°, 3°, 4°, and 5° from the grid for Spirit. Models were completed over the entire random grid, and a comparison was made by looking at log intensity and scaling it to match.

It was shown that all parameters affected the brightness, but there was a specific smaller degree of sensitivity when using partial derivatives. By altering which parameters are varied and which parameters are kept static, either boundary layer

structure sensitivity or particle size sensitivity can be chosen. If the scattering angle (the closest line angle from the observation spot to the sun) is kept constant while varying the two elevations, particle size will have little influence and boundary layer sensitivity will dominate. With the sun at a higher elevation, $\frac{\partial[\ln(I)]}{\partial[P]}$ where P is phase, could be examined to determine particle size parameter constraints as was initially attempted by the original one-layer well-mixed model. Prior research showed that $\frac{\partial[\ln(I)]}{\partial[t]}$, which is the same as $\frac{\partial[\ln(I)]}{\partial[\Theta_s]}$ where θ_s is the solar elevation angle, is inherently sensitive to the boundary layer during twilight and is sensitive to higher elevations as the sun goes below the horizon (Mark Lemmon, personal communication). Viewing the same image (which will be at a single solar elevation) while looking across at increasing scattering angle will result in particle size sensitivity. This can be utilized to emphasize the boundary layer using the same imaging data as is used for the particle size parameter constraints. For the non-continuous measurements used for the modeling parameters, $\frac{\partial[\ln(I)]}{\partial[\Theta_s]}$ is also the same as using $\partial[\ln(x)] = \frac{\partial[x]}{x}$ in the model.

A point in the sky from each image in the rover sequences is analyzed in all of the model cases to determine how the brightness and time-rate change of brightness is controlled by the different parameters. This can be done using linear regression. From this point it will be determined which parameters control which observable, and the

resulting elevations and azimuths for those parameters can then be matched up to specific observations made by each of the MERs.

The Monte Carlo code produces the model that is then compared to the data for the Sols, and an error is calculated. Error from all of the model runs are calculated using two ways of measuring the error – time-rate change (PBL sensitive) and then spatial and time-rate change (more particle size sensitive). Each was converted to a reduced chi-squared parameter so that a value near one is acceptable (about one sigma) while values far from one are not. This allows for the exclusion of models with very high error values. Overall results from error analysis include a PBL height estimation for each MER as well as generalized particle size information for each of the two different MER sites.

4. RESULTS AND DISCUSSION

Figure B7 shows a goodness of fit variation with delta for the entire set of Opportunity Sol 695 model runs. Fits in the range of ~3.5≤ delta ≤9.0 show a good fit. This goodness of fit is determined by utilizing a reduced chi-squared with normalization to unity for best fit. A lack of smooth monotonic appearance in the plot is due to a free parameter range of five different parameters and inherent noise within the Monte Carlo model itself. All model runs are shown as diamonds in the plot, with the red diamonds representing parameters other than delta occurring within their optimal values. From this a determination can be made that the model dust discontinuity is of order 5 times greater at the base of the free atmosphere compared to the top of the boundary layer. The actual atmospheric structure may not have a true discontinuity, or may have small scale local variability in the height and magnitude of the discontinuity, but these are not resolved by the model.

Figure B8 shows how the goodness of fit varies with boundary layer height (Z_{lay}) instead of delta for the sol data for Opportunity. Altitudes of 10-20 km show the best fit, although the top is poorly constrained. Boundary layer thicknesses of 4-8 km are excluded, although the observations were made at the time of day of maximum thickness.

Figure B9 shows goodness of fit versus free atmospheric scale height (H_{free}) for the Sol 659 Opportunity data. This parameter is not well constrained by the data,

although the few trials of large values did not provide good fits, showing a range of fits from the model of 5 – 11.5 km without a range of definite exclusions.

Plots shown in Figures B10 and B11 show goodness of fit versus effective radius (*a*) and effective variance (*b*) for the same Sol 695 data. For (*a*) the best fit is from 1.6 – 2.3 with worst fit from 1.0 – 1.6 microns, and for (*b*) the best fit is from 0.6 – 1.3 with the worst fit from 0.15 – 0.5. This constrains the effective particle radius at larger values for the Opportunity site, and effective variance to higher ranges as well. A larger b value results in a wider Hansen-gamma distribution, which in turn limits the amount of useful information using this particular distribution.

In Figure B12, a map of model runs is shown in *delta* vs. Z_{lay} space. All model runs are shown as plus signs. Models with parameters other than delta and boundary layer height (Z_{lay}) near optimal values are represented by diamonds. Model runs showing adequate fit are shown in red with successively worse fits being shown in green, blue, and black in order to give a sense of contours. The shaded region shows parameter values that give an elevation-airmass relation that fits Lemmon et al. (manuscript in preparation, 2010) observation of low-elevation Sun images. The intersection of the region of good fits and the shaded region suggests that a discontinuity of approximately 4 with a boundary layer height of about 10-15 km is the best model.

The next series of figures shows equivalent results plots for Spirit. Figure B13 shows the goodness of fit variation with delta for the entire set of Spirit Sol 1959 model runs. A range of delta<1 show the best fit for this parameter. Figure B14 shows the goodness of fit varying with boundary layer height instead of delta for the sol data for

Spirit, with best fit in the range of 2 –15 km and worst fit in the range from 15 – 20 km. Figure B15 varies goodness of fit with free atmospheric scale height for the Sol 1959 Spirit data, and again this parameter is not well constrained by the data. There is a range of fits from the model of 5 – 12 km without a range of definite exclusions. Plots shown in Figures B16 and B17 vary goodness of fit with (*a*) and (*b*) for the same Sol 1959 data. For (*a*) the best fit is from 2.2 – 2.8 microns with worst fit from 1.3 – 2.0 microns, and for (*b*) the best fit is from 1.0 – 1.4 with the worst fit from 0.175 – 0.7. Figure B18 shows how the representative modeled results for these particle-size parameters for the Spirit data (a=2.4 microns, b=1.2) compare to size distributions of previous studies. In each case, the contribution of extinction from each particle size is shown. Again, the larger variance values affect the width of the Hansen-gamma distribution, which in turn leads to a possibility that another distribution type would provide better, more constrained results. In addition, the particle sizes are skewed to both large and small values while deprecating values in the middle of the range. The overall shape of the curve for this study is wider than some of the other curves, but it is almost on top of the Clancy et al., 1995 curve. Note that, first, the Spirit model is similar to the previous wide distributions; and second, all of the distributions are similar near their modal sizes, and the difference is in relative contributions from the extremes. In fact, the Spirit models large size is not as apparent in the figure as is its large variance.

In Figure B19, a map of fit quality for boundary layer parameters is shown. Note that in this case, the assumed free atmosphere scale height is almost the same as the scale height measured by Lemmon et al. (manuscript in preparation, 2010) for the whole

atmosphere, so the constraint suggests little to no discontinuity at any altitude. The best fits for the scattering model show increasing delta for lower altitudes. While the model resolution is somewhat lost below 2 km (thus no model runs were attempted), the suggestion is that the boundary layer assumptions may be violated. The model seems to be pushing toward a uniform atmosphere with a scale height below the one assumed for the boundary layer.

The two separate sites for the MERs revealed different PBL characteristics due to a difference in optical depths for the two sites on the Sols studied. For Opportunity, the results show a 5x – 10x dust enhancement at altitudes of 10-15 km, while very different conditions were seen by Spirit. A cleaner boundary layer at the Opportunity site is not especially surprising. The area appears dark from orbit, suggesting a relatively dust free surface. Images on the ground confirm this, and show dark, sand-sized particles instead. In addition, dust deposits slowly on Opportunity and is cleaned by winds frequently (Mark Lemmon, personal communication). On the other hand, the boundary layer is relatively dustier at the Spirit site, where the surface is bright and obviously dusty in surface images. Sedimentation of dust onto solar panels is also faster, with cleaning events rarer, at the Spirit site.

The models of both sites suggest large particles and wide size distributions. The Spirit data are the most conclusive due to the longer imaging sequence that was available. Large particles are not surprising given that both data sets were taken in the aftermath of dust storms, with dust still settling out of the atmosphere. The wide distributions ($b>1$) are slightly problematic. First, while some investigators have also

suggested wide distributions (Toon et al. 1977, Clancy et al. 2003), many have not. Again, following a dust storm there may be a wider range in particle size than after all the large particles have settled. Second, while b>1 is physical, it makes the distribution so wide that a Hansen-gamma distribution is probably not the best. However, it is unlikely there is sufficient data to test not only the mean and variance of the distribution, but to also test the detailed shape.

5. CONCLUSIONS

This study utilized MER Pancam twilight imaging datasets during Sol 1959 (Spirit) and Sol 695 (Opportunity) to measure the height of the PBL and size of the discontinuity in dust within and above the boundary layer based upon the decay of a Martian dust storm. General particle size ranges were also found. Even though there are modeled results utilizing PBL density LIDAR profiles from Phoenix and PBL temperature profiles utilizing Mini-TES data from the MERs, the two datasets are not from the same site. In addition, previously modeled results utilizing other datasets have been lacking in actual ground-based measurements for verification of PBL characteristics.

- The PBL measurements are dependent on geodetic altitude, and MER observations are biased to lower altitudes, which in turn likely results in thicker PBL results than if the MERs were at a higher altitude at a different site on Mars (Lemmon et al., 2004a; Spiga et al., 2010). In addition, Spirit's site was extremely dusty where dust storms can originate, but Opportunity's site was relatively dust-free with dust storms blowing through the area (Lemmon et al., 2004a). Also, as seen in the schematic in Figure B20, the Spirit site appears to have a negative discontinuity while Opportunity shows a positive discontinuity. This knowledge combined with the results from this study can be used to plan

future missions in order to obtain as much information about the Martian PBL as possible.

- Previous interpretations of IR measurements from global optical depth datasets utilize a well-mixed dust profile down to the boundary layer. It is possible that changes in IR-to-visible ratios shown by Wolff et al., 2006 are due to the fact that the dust is not well-mixed. Any interpretation of thermal emission datasets based upon the well-mixed assumption may also be incorrect if the dust is above or below this estimation and is therefore warmer or cooler than estimated, resulting in strong systematic errors in measurements of Mars climatology. It is plausible that previous studies based on a single well-mixed atmospheric layer could benefit from being reassessed using multiple layers and ground-truthed PBL heights.
- The twilight-imaging method can measure PBL characteristics at different rover sites with different optical depths while also providing insight into dust particle parameter measurements utilizing currently available datasets. Both rovers have taken several twilight sequences, and the sequences taken within the 1900-2000 timeframe were influenced by results from preliminary work in this study. MER datasets are already relatively numerous and mostly publicly available, and refinement of this study's approach will allow for a better overall view of the Martian PBL and dust parameters.

- Results from this study can be used to recommend a strategy for probing boundary layer structure during future Mars missions that will be able to focus on adding to the datasets for the twilight imaging sequences for different time periods and dust-loading situations. While one of the rovers is currently out of operation, the other is able to continue imaging, and there is always hope that the out-of-operation rover will be functional again in the future.
- Changes in dust loading following local and global storms can be used to better model the dynamics of the Martian PBL, and this in turn can help climate modelers build more robust Martian GCMs.
- Measurements to constrain similar models should include a time series of images near the setting (or rising) Sun in at least one short wavelength filter. The time series should span a wide range of solar elevations similar to the Spirit sequence rather than the Opportunity sequence, and they should optimally be used to study pre- and post- dust storm skies. Such a pair of observations is tentatively planned for Opportunity in the weeks before and after the anticipated start of dust storm season (Mark Lemmon, personal communication).

Overall this study provides a unique approach to determining characteristics of both the Martian PBL and dust characteristics. The inclusion of additional datasets in continued research will provide a more robust solution to the issue of incorrectly

assumed well-mixed dust layer properties utilized in many previous models. This in turn will provide an improved general representation of the atmosphere on Mars.

REFERENCES

Adams, C.N., and G. W. Kattawar (1978), Radiative transfer in spherical shell atmospheres – 1. Rayleigh scattering, *Icarus, 35,* 139-151.

Beaty, D.W., K. Snook, C.C. Allen, D. Eppler, W.M. Farrell, et al. (2005), An analysis of the precursor measurements of Mars needed to reduce the risk of the first human missions to Mars, Unpublished white paper, 77p, Mars Exploration Program Analysis Group, http://sirius.bu.edu/withers/pppp/pdf/beaty2005.pdf.

Bell, J.F. III, S.W. Squyres, K.E. Herkenhoff, J.N. Maki, H.M. Arneson, et al. (2003), Mars Exploration Rover Athena Panoramic Camera (Pancam) investigation, *J. Geophys. Res.*, *108*, ROV 4-1 – 4-30.

Bell, J.F. III, S.W. Squyres, R.E. Arvidson, H.M. Arneson, D. Bass, et al. (2004a), Pancam multispectral imaging results from the Spirit rover at Gusev Crater, *Science*, *305*, 800-806.

Bell, J.F. III, S.W. Squyres, R.E. Arvidson, H.M. Ameson, D. Bass, et al. (2004b), Pancam multispectral imaging results from the Opportunity rover at Meridiani Planum, *Science*, *306*, 1703-1709.

Blumsack, S.L., P.J. Gierasch, and W.R. Wessel (1973), An analytical and numerical study of the Martian planetary boundary layer over slopes, *Journal of Atmospheric Sciences*, *30*, 66-82.

Christensen, P.R., M.B. Wyatt, T.D. Glotch, A.D. Rogers, S. Anwar, et al. (2004), Mineralogy at Meridiani Planum from the Mini-TES experiment on the Opportunity Rover, *Science*, *306*, 1733-1739.

Clancy, R.T., S.W. Lee, G.R. Gladstone, W.W. McMillan, and T. Rousch (1995), A new model for Mars atmospheric dust based upon analysis of ultraviolet through infrared observations from Mariner 9, Viking, and Phobos, *Journal of Geophysical Research*, *100* (E3), 5251-5263.

Clancy, R.T., M.J. Wolff, and P.R. Christensen (2003), Mars aerosol studies with the MGS TES emission phase function observations; Optical depths, particle sizes, and ice cloud types versus latitude and solar longitude, *J. Geophys. Res. (Planets)*, *108*, 2-1 – 2-20.

Collins, D. G., W. G. Blättner, M. B. Wells, and H. G. Horak (1972), Backward Monte Carlo calculations of the polarization characteristics of the radiation emerging from spherical-shell atmospheres, *Applied Optics, 11*(11)*,* 2684-2696.

Conrath, B.J. (1975), Thermal structure of the Martian atmosphere during the dissipation of the dust storm of 1971, *Icarus*, *24*, 36-46.

Daerden, F., J.A. Whiteway, R. Davy, C. Verhoeven, L. Komguem, et al. (2010), Simulating observed boundary layer clouds on Mars, *Geophysical Research Letters*, *37*, L04203, 5pp.

Davy, R., P.A. Taylor, W. Weng, and P.-Y. Li (2009), A model of dust in the Martian lower atmosphere, *Journal of Geophysical Research*, *114*, D04108.

Davy, R., J.A. Davis, P.A. Taylor, C.F. Lange, W. Weng, et al. (2010), Initial analysis of air temperature and related data from the Phoenix MET station and their use in estimating turbulent heat fluxes, *Journal of Geophysical Research*, *115*, E00E13.

Gierasch, P.J., and R.M. Goody (1968), A study of the thermal and dynamical structure of the Martian lower atmosphere, *Planetary Space Science*, *16*, 615-646.

Gierasch, P.J., and R.M. Goody (1972), The effect of dust on the temperature structure of the Martian atmosphere, *J. Atmos. Sci.*, *29*, 400-402.

Haberle, R.M., C.B. Leovy, and J.B. Pollack (1982), Some effects of dust storms on the global circulation of Mars, *J. Atmos. Sci.*, *50*, 322-367.

Haberle, R.M, J.B. Pollack, J.R. Barnes, R.W. Zurek, C.B. Leovy, et al. (1993), Mars atmospheric dynamics as simulated by the NASA Ames general circulation model, 1, The zonal-mean circulation, *Journal of Geophysical Research*, *98*, 3093-3123.

Hartmann, W.K., and M.J. Price (1974), Mars: Clearing of the 1971 dust storm, *Icarus*, *21*, 28-34.

Hess, S. L., R. M. Henry, C. B. Leovy, J. A. Ryan, and J. E. Tillman (1977), Meteorological results from the surface of Mars: Viking 1 and 2, *J. Geophys. Res.*, *82*, 4559–4574.

Hinson, D. P., R. A. Simpson, J. D. Twicken, G. L. Tyler, and F. M. Flasar (1999), Initial results from radio occultation measurements with Mars Global Surveyor, *J. Geophys. Res.*, *104*, 26,997– 27,012.

Hinson, D. P, G. L. Tyler, J. L. Hollingsworth, and R. J. Wilson (2001), Radio Occultation Measurements of Forced Atmospheric Waves on Mars, *J. Geophys. Res.*, *106*, 1463.

Hinson, D. P., M. D. Smith, and B. J. Conrath (2004), Comparison of atmospheric temperatures obtained through infrared sounding and radio occultation by Mars Global Surveyor, *Journal of Geophysical Research*, *109*, E12002.

Hinson, D.P., M. Patzold, S. Tellman, B. Hausler, and G.L. Tyler (2008), The depth of the convective boundary layer on Mars, *Icarus*, *198*, 57-66.

Johnson, J.R., W.M Grundy, and M.T. Lemmon (2003), Dust deposition at the Mars Pathfinder landing site: observations and modeling of visible/near-infrared spectra, *Icarus*, *163* (2), 330-346.

Kahn, R., and R. Goody (1981), The Martian twilight, *Journal of Geophysical Research*, *86*(A7), 5833-5838.

Kahn, R.A., T.Z. Martin, R.W. Zurek, and S.W. Lee (1992), The Martian dust cycle, in *Mars*, ed. H. Kieffer *et al.*, pp. 1017-1053, Univ. Arizona Press, Tucson.

Kliore, A. J., G. Fjeldbo, B. L. Siedel, M. J. Sykes, and P. M. Woiceshyn (1973), S band radio occultation measurements of the atmosphere and topography of Mars with Mariner 9: Extended mission coverage of polar and intermediate latitudes, *J. Geophys. Res.*, *78*, 4331– 4351.

Korablev, O., V.I. Moroz, E.V. Petrova, and A.V. Rodin (2005), Optical properties of dust and the opacity of the Martian atmosphere, *Advances in Space Research*, *35*(1), 21-30.

Larsen, S.E., H.E. Jorgensen, L. Landberg, and J.E. Tillman (2002), Aspects of the atmospheric surface layers on Mars and Earth, *Boundary-Layer Meteorology*, *105*(3), 451-470.

Lemmon, M.T., M.J. Wolff, M.D. Smith, R.T. Clancy, D. Banfield, et al. (2004a), Atmospheric imaging results from the Mars Exploration Rovers: Spirit and Opportunity, *Science*, *306*, 1753-1756.

Lemmon, M.T. (2004b), MER Mars Pancam Atmospheric Opacity RDR V1.0, NASA Planetary Data System, MER-M-PANCAM-5-ATMOS-OPACITY-V1.0.

Lindal, G. F., H. B. Hotz, D. N. Sweetnam, Z. Shippony, J. P. Brenkle, et al. (1979), Viking radio occultation measurements of the atmosphere and topography of Mars: Data acquired during 1 Martian year of tracking, *J. Geophys. Res.*, *84*, 8443–8456.

Maattanen, A., and H. Savijarvi (2004), Sensitivity tests with one-dimensional boundary-layer Mars model, *Boundary-Layer Meteorology*, *113*, 305-320.

Magalhaes, J., and P. Gierasch (1982), A model of Martian slope winds: Implications for Aeolian transport, *Journal of Geophysical Research*, *87*, 9975-9984.

Markiewicz, W.J., R.M. Slabotny, H.U. Keller, N. Thomas, D. Titov, and P.H. Smith (1999), Optical properties of the Martian aerosols as derived from Imager for Mars Pathfinder midday sky brightness data, *J. Geophys. Res.*, *104*, 9009-9017.

Martinez, G., F. Valero, and L. Vazquez (2009), Characterization of the Martian convective boundary layer, *Journal of the Atmospheric Sciences*, *66*, 2044-2058.

Odaka, M. (2001), A numerical simulation of Martian atmospheric convection with a two-dimensional anelastic model: A case of dust-free Mars, *Geophys. Res. Lett.*, *28*, 895-898.

Pollack, J.B., S. Colburn, F.M. Flaser, R. Kahn, C.E. Carlson, and D.C. Pidek (1979), Properties and effects of dust suspended in the Martian atmosphere, *J. Geophys. Res.*, *84*, 2929-2945.

Pollack, J.B., and J.N. Cuzzi (1980), Scattering by nonspherical particles of size comparable to a wavelength: a new semi-empirical theory and application to tropospheric aerosols, *Journal of the Atmospheric Sciences*, *35*, 868.

Pollack, J.B, M.E. Ockert-Bell, and M.K. Shepard (1995), Viking Lander image analysis of Martian atmospheric dust, *J. Geophys. Res.*, *100*, 5235-5250.

Rafkin, S., R. Haberle, and T. Michaels (2001), The Mars regional atmospheric modeling system: Model description and selected simulations, *Icarus*, *151*, 228-256.

Savijarvi, H. (1991a), Radiative fluxes on a dustfree Mars, *Contr. Atmos. Phys.*, *64*, 103-112.

Savijarvi, H. (1991b), A model study of the PBL structure on Mars and the Earth, *Contr. Atmos. Phys.*, *64*, 219-229.

Savijarvi, H. (1995), Mars boundary layer modeling: diurnal moisture cycle and soil properties at the Viking Lander 1 site, *Icarus*, *117*(1), 120-127.

Savijarvi, H. (1999), A model study of the atmospheric boundary layer in the Mars Pathfinder lander conditions, *Quarterly Journal of the Royal Meteorological Society*, *125*, 483-493.

Savijarvi, H. and T. Siili (1993), The Martian slope winds and the nocturnal PBL jet, *J. Atmos. Sci.*, *50*, 77-88.

Savijarvi, H., A. Maattanen, J. Kauhanen, and A. Harri (2004), Mars Pathfinder: New data and new model simulations, *Quarterly Journal of the Royal Meteorological Society*, *130*, 669-683.

Savijarvi, H., and J. Kauhanen (2008), Surface and boundary-layer modeling for the Mars Exploration Rover sites, *Quarterly Journal of the Royal Meteorological Society*, *134*, 635-641.

Schofield, J. T., J. R. Barnes, D. Crisp, R. M. Haberle, S. Larsen, et al. (1997), The Mars Pathfinder atmospheric structure investigation/meteorology (ASIMET) experiment, *Science*, *278*, 1752– 1758.

Seiff, A., and D. B. Kirk (1977), Structure of the atmosphere of Mars in summer at mid-latitudes, *J. Geophys. Res.*, *82*, 4364–4378.

Sharma, R., D.W. Clark, P.K. Srirama, and M.K. Mazumder (2008), Tribocharging characteristics of the Mars dust stimulant (JSC Mars-1), *IEEE Transactions on Industry Applications*, *44* (1), 32-39.

Siili, T., R. Haberle, and J. Murphy (1997), Sensitivity of Martian southern polar cap edge winds and surface stresses to dust optical thickness and to the large-scale sublimation flow, *Adv. Space Res.*, *19*, 1241-1244.

Smith, M.D. (2008), Spacecraft observations of the Martian atmosphere, *Annual Review of Earth and Planetary Sciences*, *36*, 191-219.

Smith, M.D., M.J. Wolff, N. Spanovich, A. Ghosh, D. Banfield, et al. (2006), One Martian year of atmospheric observations using MER Mini-TES, *Journal of Geophysical Research*, *111*(E12s13).

Smith, P.H., and M. Lemmon (1999), Opacity of the Martian atmosphere measured by the images for Mars Pathfinder, *J. Geophys. Res.*, *104*(E4), 8975-8985.

Sorbjan, Z. (2007a), Statistics of shallow convection on Mars based on large-eddy simulations – Part 1: shearless conditions, *Boundary-Layer Meteorology*, *123*, 121-142.

Sorbjan, Z. (2007b), Statistics of shallow convection on Mars based on large-eddy simulations – Part 2: effects of wind shear, *Boundary-Layer Meteorology*, *123*, 143-157.

Sorbjan, Z., M. Wolff, and M.D. Smith (2009), Thermal structure of the atmospheric boundary layer on Mars based on Mini-TES observations, *Quarterly Journal of the Royal Meteorological Society*, *135*, 1776-1787.

Spiga, A., and F. Forget (2009), A new model to simulate the Martian mesoscale and microscale atmospheric circulation: Validation and first results, *Journal of Geophysical Research*, *114*, E02009.

Spiga, A., F. Forget, S.R. Lewis, and D.P. Hinson (2010), Structure and dynamics of the convective boundary layer on Mars as inferred from large-eddy simulations and remote-sensing measurements, *Quarterly Journal of the Royal Meteorological Society*, DOI:10.1002/qj.563.

Sutton, J. L., C. B. Leovy, and J. E. Tillman (1978), Diurnal variations of the Martian surface layer meteorological parameters during the first 45 sols at two Viking lander sites, *J. Atmos. Sci.*, *35*, 2346–2355.

Taylor, P.A., P.-Y. Li, D.V. Michelangeli, J. Pathak, and W. Weng (2007), Modelling dust distributions in the atmospheric boundary layer on Mars, *Boundary-Layer Meteorology*, *125*, 305-328.

Toigo, A. D., and M. I. Richardson (2002), A mesoscale model for the Martian atmosphere, *J. Geophys. Res.*, *107*(E7), 5049, doi:10.1029/2000JE001489

Tomasko, M.G., L.R. Doose, M. Lemmon, P.H. Smith, and E. Wegryn (1999), Properties of dust in the Martian atmosphere from the Imager on Mars Pathfinder, *J. Geophys. Res.*, *104*, 9009-9017.

Toon, O.B., J.B. Pollack, and C. Sagan (1977), Physical properties of the particles composing the martian dust storm of 1971 – 1972, *Icarus*, *30*, 663-696.

Vincendon, M. (2008a), Dust aerosols above the south polar cap of Mars as seen by OMEGA, *Icarus*, *196*(2), 488-505.

Vincendon, M. (2008b), Yearly and seasonal variations of low albedo surfaces on Mars in the OMEGA/MEx dataset: Constraints on aerosols properties and dust deposits, *Icarus*, *200*(2), 395-405.

Wallace, J.M., and P.V. Hobbs (2006), *Atmospheric Science – Second Edition, An Introductory Survey*, Academic Press, New York.

Whiteway, J.A., L. Komguem, C. Dickinson, C. Cook, M. Illnicki, et al. (2009), Mars water-ice clouds and precipitation, *Science*, *325*, 68.

Wolff, M.J, and R.T. Clancy (2003), Constraints on the size of martian aerosols from Thermal Emission Spectrometer observations, *J. Geophys. Res. (Planets)*, *108*, 1-1 – 1-23.

Wolff, M.J., M.D. Smith, R.T. Clancy, N. Spanovich, B.A. Whitney, et al. (2006), Constraints on dust aerosols from the Mars Exploration Rovers using MGS overflights and Mini-TES, *J. Geophys. Res. (Planets)*, *111*, 1-23.

Ye, Z.J., M. Segal, and R.A. Pielke (1990), A comparative study of daytime thermally induced upslope flow on Mars and Earth, *Journal of Atmospheric Science*, *47*, 612-628.

Zent, A.P., R.M. Haberle, H.C. Houben, and B.M. Jakosky (1993), A coupled subsurface-boundary layer model of water on Mars, *Journal of Geophysical Research*, *98*, 3319-3337.

APPENDIX A

Table A1 A Comparison of Parameters for Mars and Earth (adapted from Larsen, et al. 2002).

Parameter	**Units**	**Mars**	**Earth**
Gas Composition			
CO_2		95	0.035
N_2		2.7	78
O_2	% by volume	0.13	21
H_2O		0 – 0.2	0 – 4
Ar		1.6	0.9
Solar Constant	Wm^{-2}	591	1373
Orbital Eccentricity		0.093	0.017
Axial Inclination	degrees	25.2	23.4
Length of Day	hours	24.65 (1 Sol)	24.00
Length of Year	Earth days	686.98 (669 Sols)	365.26
Gravity, g	ms^{-2}	3.7	9.8
Atmospheric gas constant, R	$J\ kg^{-1}\ K^{-1}$	188	287
Typical surface pressure, p	hPa	7	1015
Typical surface density, ρ	$kg\ m^{-3}$	$1.5\ 10^{-2}$	1.2
Typical surface temperature, T	K	220	300
Scale height H=RT/g	kilometer	11.178	8.785

Table A2 Model Parameters and Descriptions for Layer Model

Model Parameter	Description
N_i	Imaginary Index of Refraction
Theta min	Internal Transmission Angle Minimum
G	Slope of the Log of the Phase Function for Internal Transmission at Angle 0°
Tau	Optical Depth
Lambda	Wavelength
SSA	Single Scattering Albedo
Altitude	Where Camera Sits Relative to Surface
N_{phot}	Number of Photons for Monte Carlo Model
W_{min}	Smallest Weight to Follow Photon To
R_ran	Random Seed Test Diagnostic
R_{pla}	Planet Radius
Fn	Phase function file name
Gr	Ground reflectivity
Wp	Single Scattering Albedo
N_{theta}	Number of Theta Values Used
Theta	Negative Solar Elevation (negative value is a positive elevation)
N_{az}	Number of Azimuths Used
Azi	Azimuth Value
N_{elev}	Number of Elevations Used
Elev	Elevation (positive value is “up”)
Num_{lay}	Number of Layers
H_{lay}	Scale Height Within Layer
Z_{lay}	Height Where Layer Starts (0 Value Starts at Ground Level)
Tau_{lay}	Tau Value for Layer
Boundl	Truncates Atmosphere

Table A3 Varied Parameter Ranges Investigated in This Study

Parameter	**Mer A – Spirit**	**Mer B - Opportunity**
Number of Trials	1294	1016
***a* range**	1.303 – 2.798 microns	1.005 – 2.396 microns
***b* range**	0.155 – 1.397	0.151 – 1.399
***Delta* range**	0.192 – 19.429	0.136 – 135.539
Z_{lay} **range**	2.069 – 24.980	2.085 – 20.982
***H1* range**	5.000 – 11.998	5.009 – 14.896

APPENDIX B

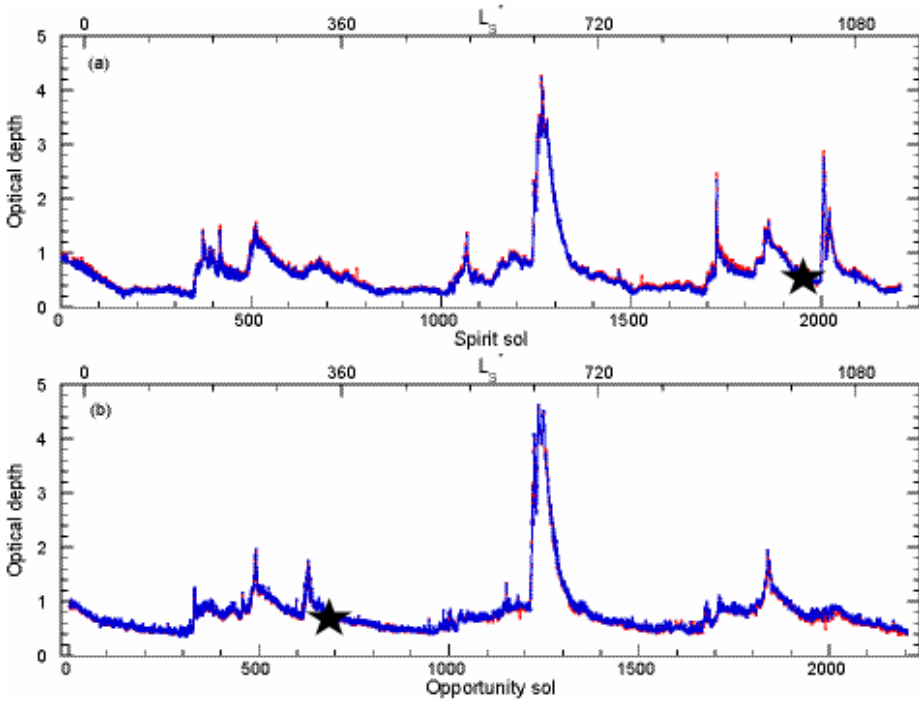

Figure B1. MER optical depth records for Spirit and Opportunity shown as a function of sol. Observed opacity for filter L8 (blue) and filter R8 (red) is shown with all valid measurements presented. The approximate optical depth for Sol 1959 (Spirit) and Sol 659 (Opportunity) are shown as black stars. An approximate L_S scale along the top axis is modified to increase through the mission (successive northern spring equinoxes are at 0°, 360°, 720°, and 1080°). (Adapted from Lemmon et al., manuscript in preparation, 2010, Figure 1)

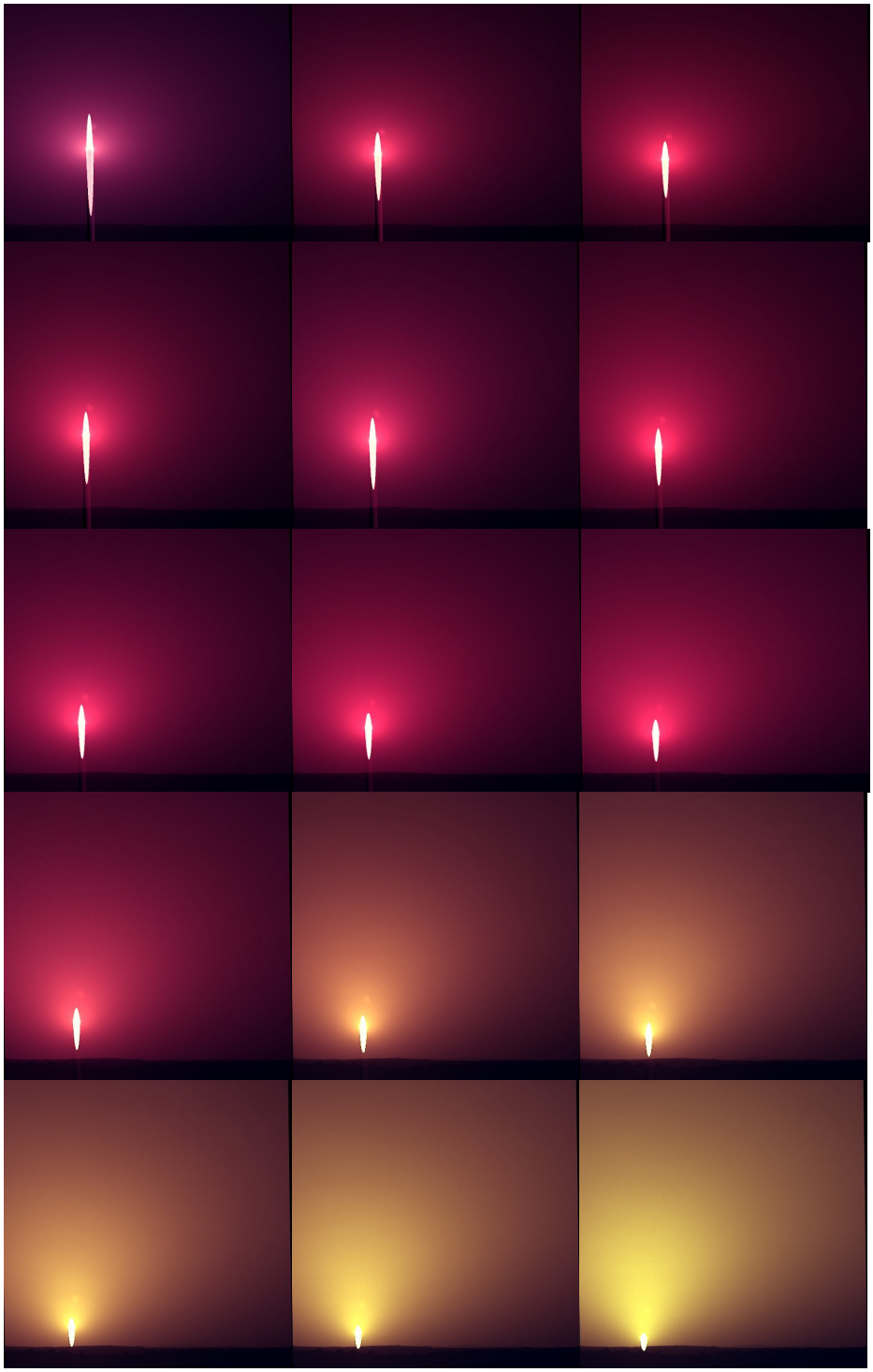

Figure B2. Spirit sol 1959 sunset images, pseudo-color. Note that the streak spreading vertically from the Sun is due to charge "bleeding" in the detector due to saturation of the Sun while exposing for the sky.

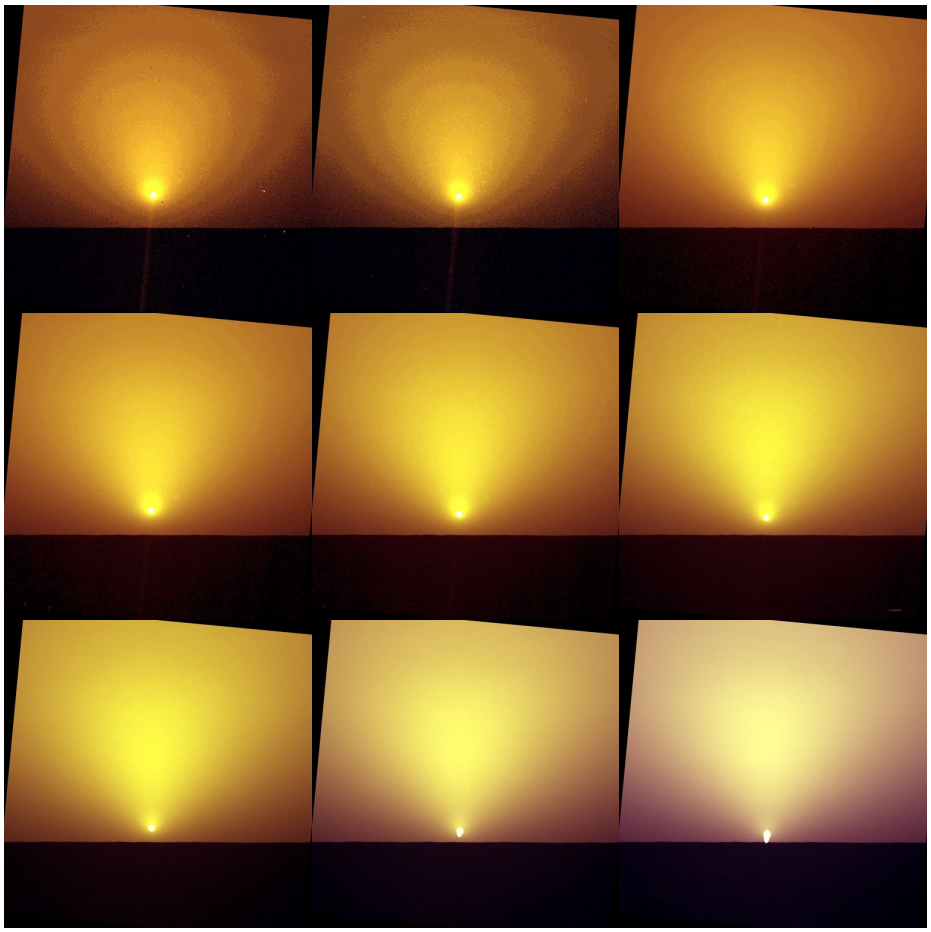

Figure B3. As for Figure B5, with Opportunity sol 695 images. The first two images show quantization effects that result from underexposure.

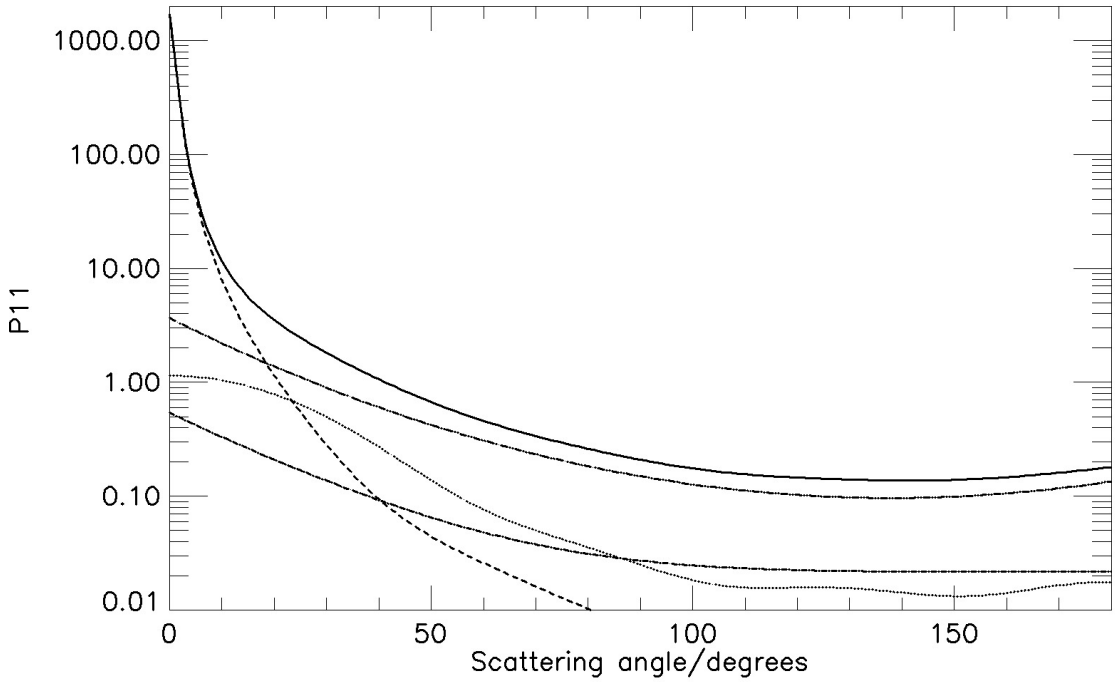

Figure B4. Phase function for irregular aerosol. The composite phase function is shown (solid line), along with model components from (in order of contribution at 0 degrees: diffraction, short dash; transmission, dash-dot-dot; small particle Mie scattering, dot; and reflection, dash-dot. Diffraction dominates completely inside 10 degrees, while the transmission prescription dominates outside of 20 degrees. Shown for λ=0.43 microns, a=2.4 microns, b=1.2, n_r=1.5, n_i=0.0101, G=115., θ_{min}=138 degrees.

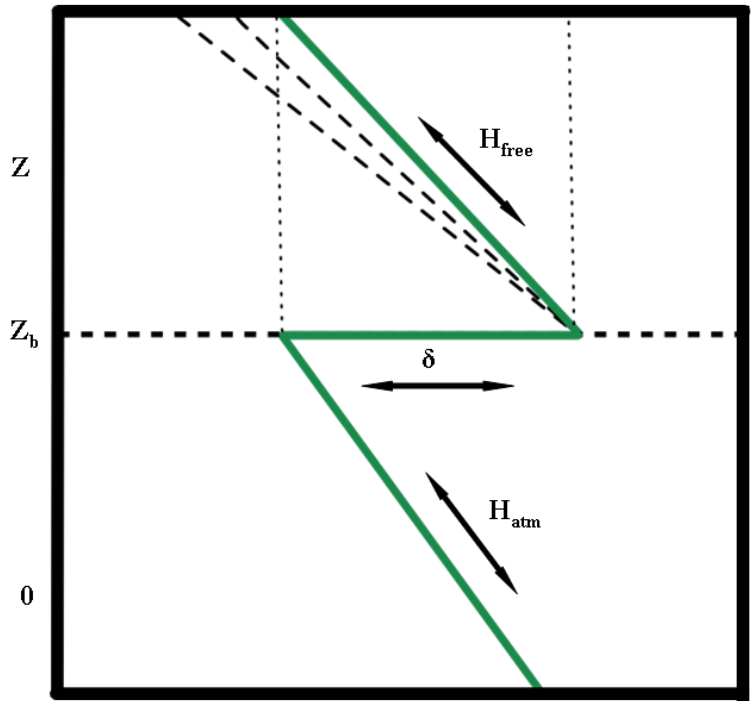

Figure B5. General schematic showing structural model used in study.

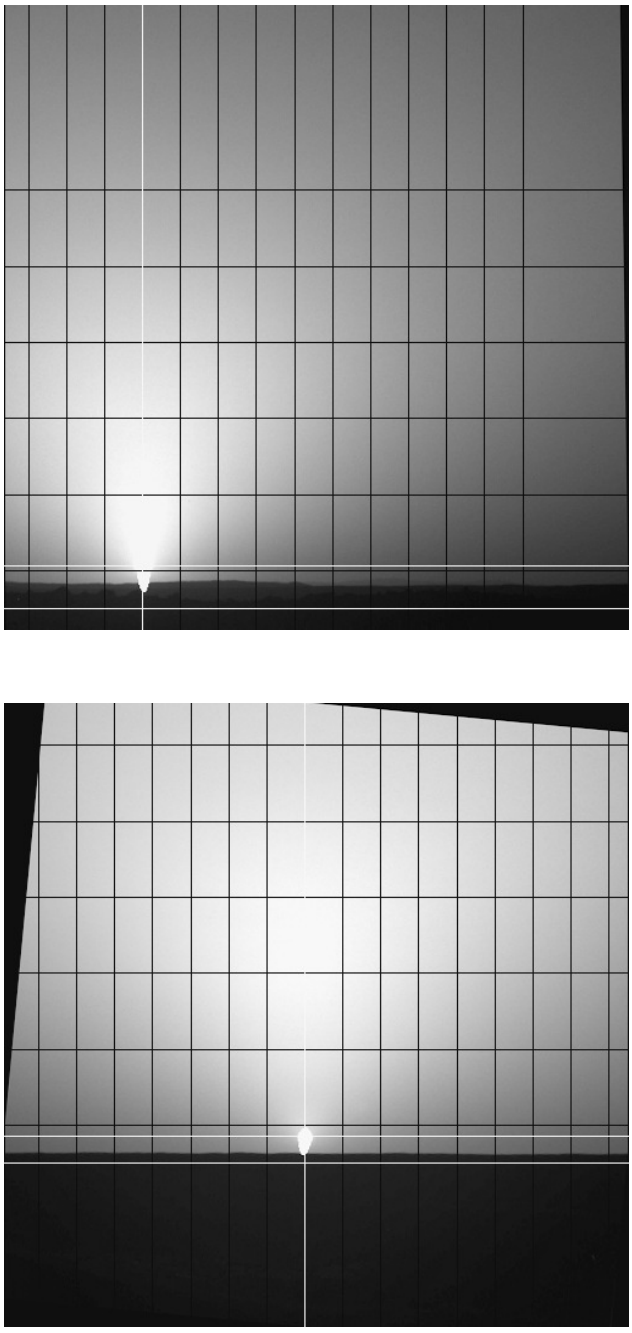

Figure B6. Images taken during the sunset sequences of (A, top image) Spirit sol 1959, solar elevation 1.1 degrees, visible optical depth 0.49; and (B, bottom image) Opportunity sol 695, solar elevation 0.7 degrees, visible optical depth 0.77. For each, violet filter (L7) images are rotated to level the true horizon, which is shown as the lower horizontal white line. The upper horizontal white line passes thought the center of the Sun, as does the vertical white line. The black lines illustrate the azimuth (+-1, 2, 3, … degrees from the Sun) and elevation (+1, 3, 5, … degrees) grid used in modeling.

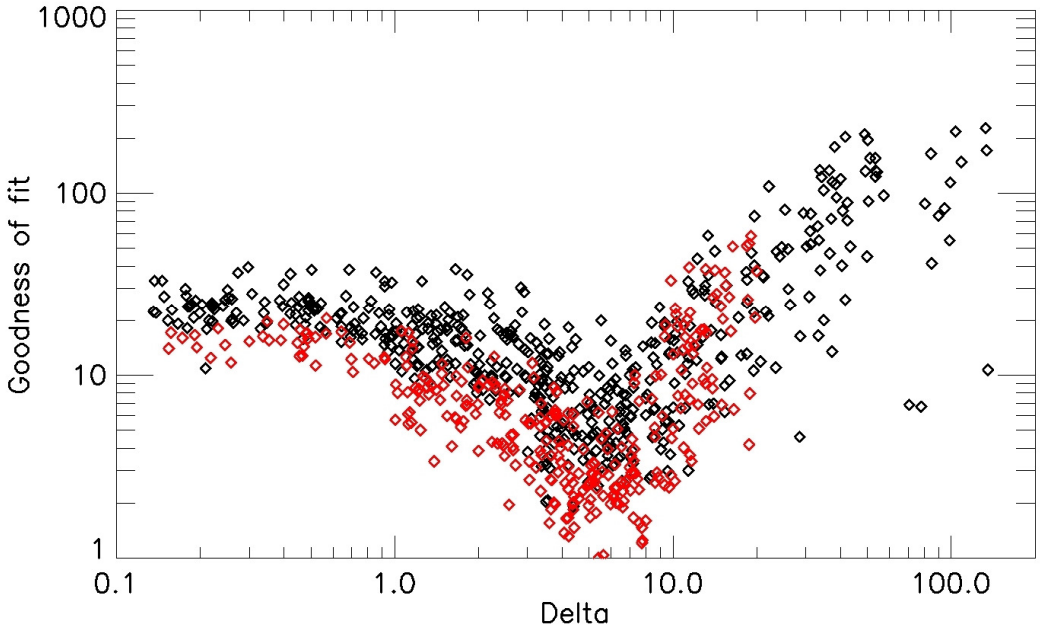

Figure B7. Goodness of fit varies with delta for all B/695 model runs. Goodness of fit is determined by reduced chi-squared with normalization to unity for the best fit (see text). Goodness of fit is not smoothly monotonic due to both the effect of 5 free parameters and the fact that the Monte Carlo model itself adds noise. Diamonds show all model runs; those in red show runs where parameters other than delta are near their optimal values.

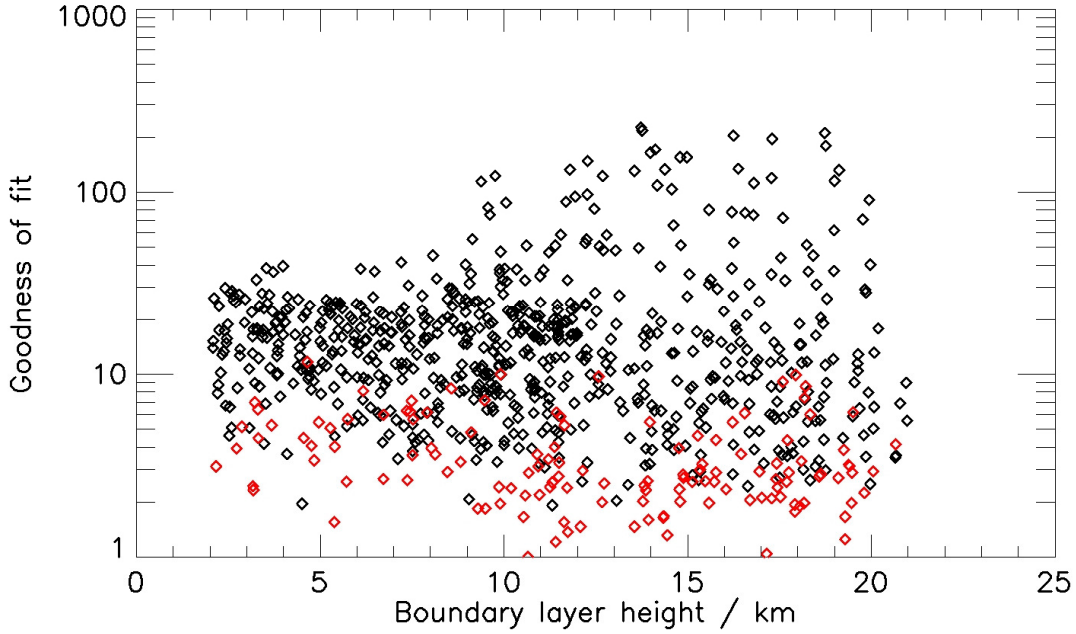

Figure B8. As Figure B7, except goodness of fit varies with boundary layer height for all B/695 model runs.

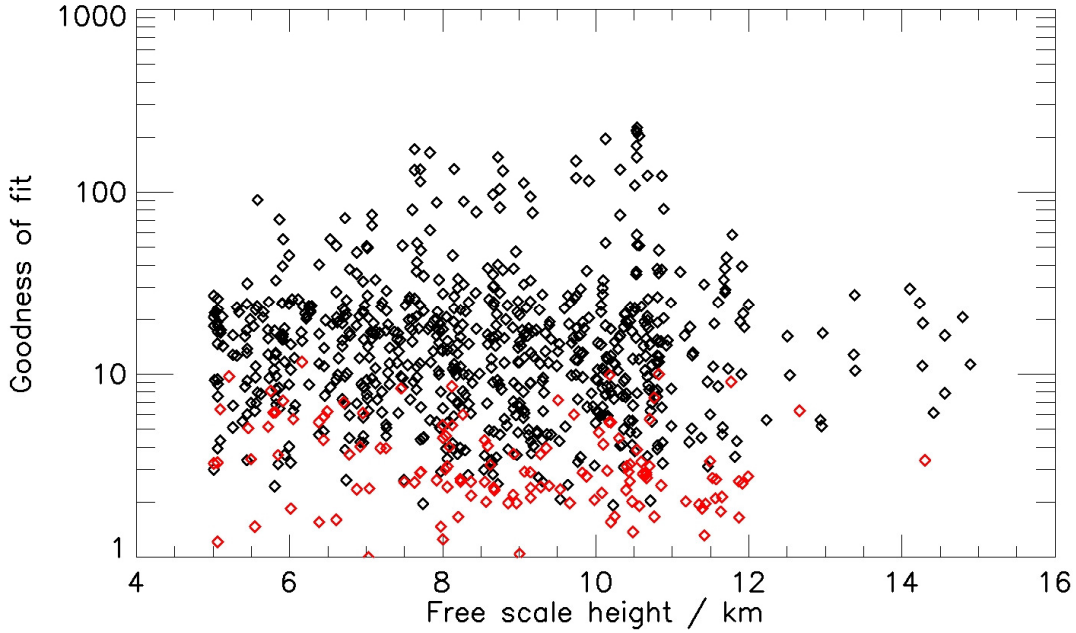

Figure B9. As Figure B7, except goodness of fit varies with free-atmosphere scale height for all B/695 model runs.

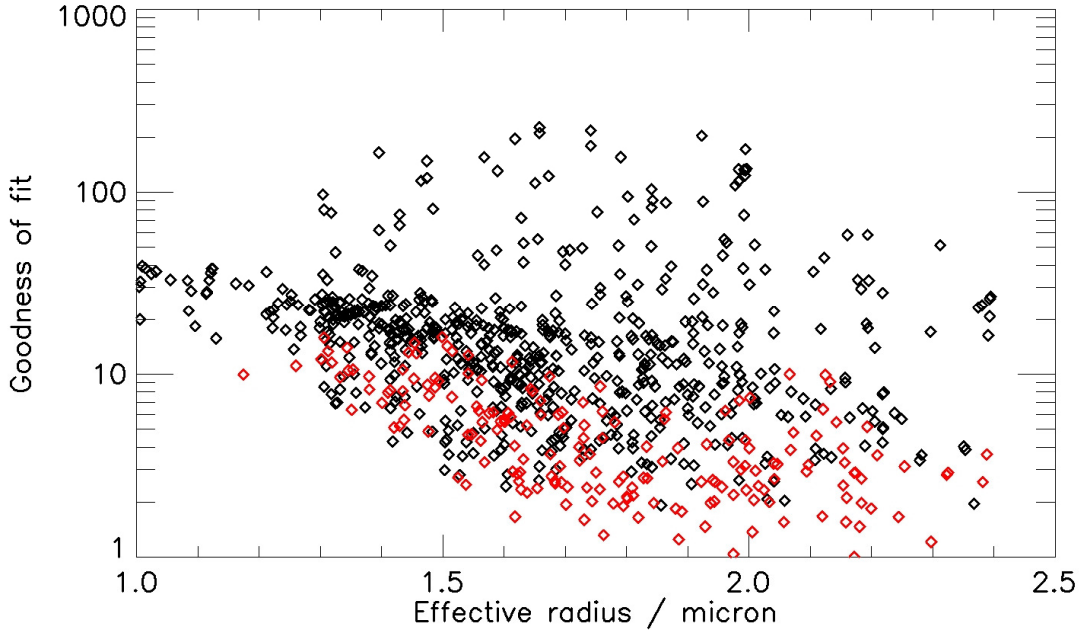

Figure B10. As Figure B7, except goodness of fit varies with effective radius for all B/695 model runs.

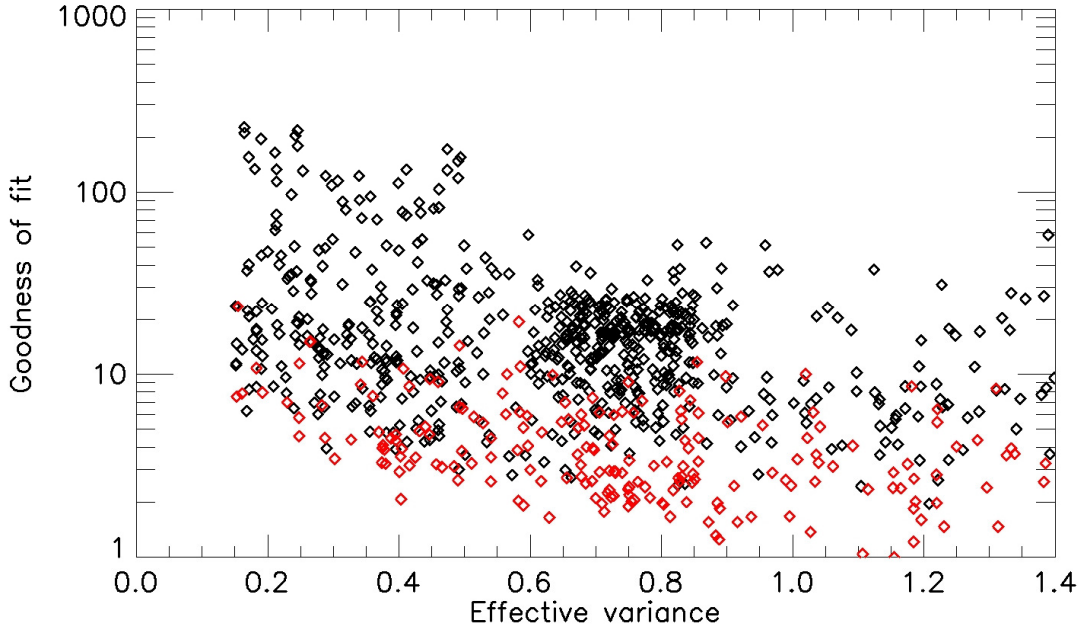

Figure B11. As Figure B7, except goodness of fit varies with effective variance for all B/695 model runs.

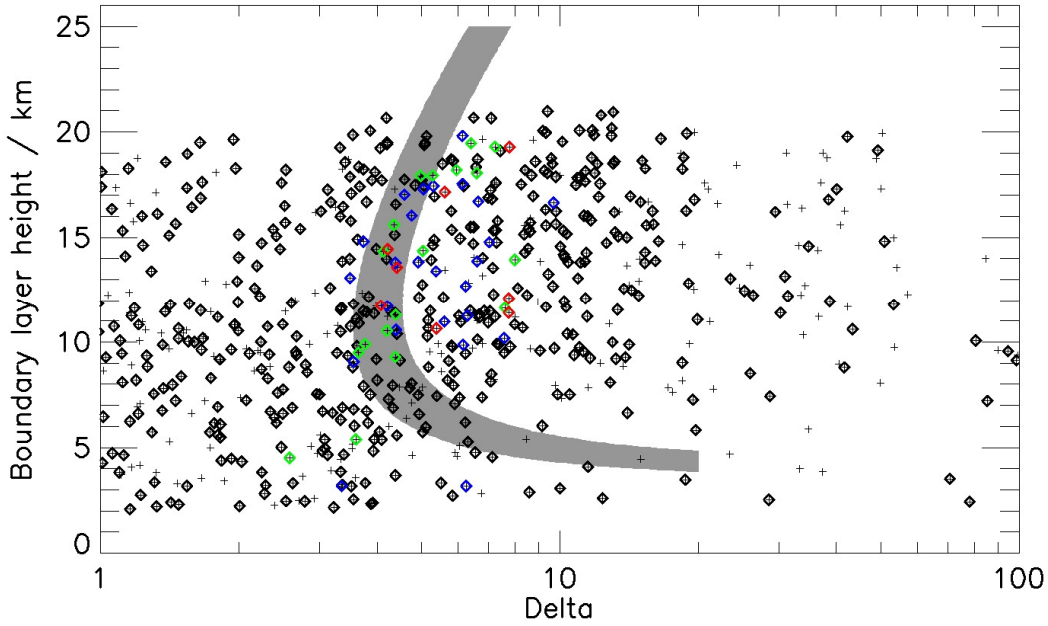

Figure B12. Map of fit quality for boundary layer parameters for B/695. All model runs are shown with plus signs. Model runs where parameters other than delta and boundary layer height were near optimal are shown with diamonds. Model runs with adequate fits are shown in red; to give a sense of contours, model runs with successively worse fits are shown in green, blue, and black.

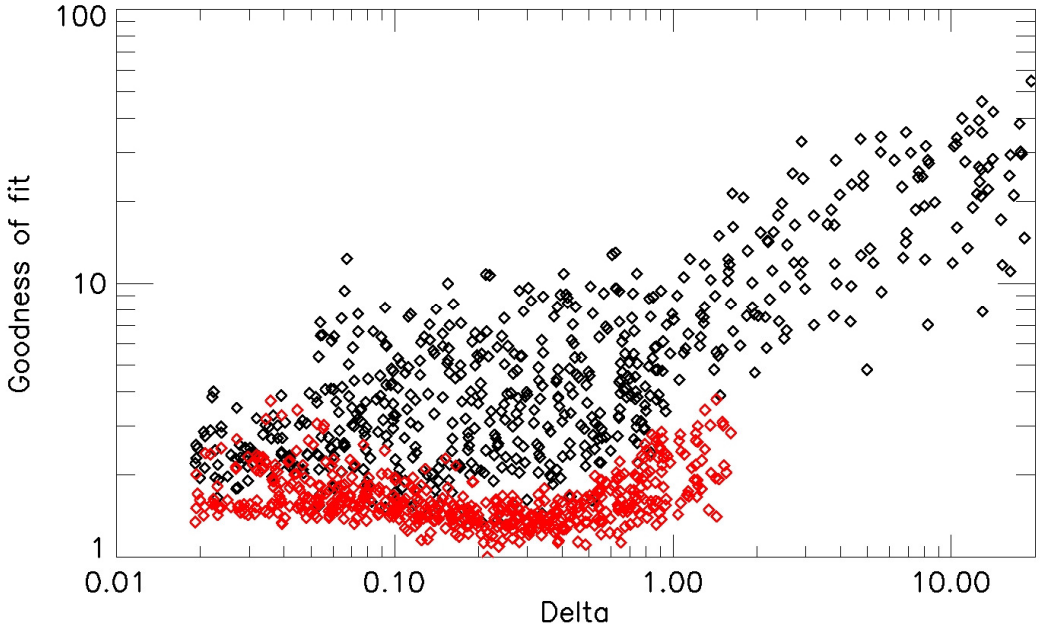

Figure B13. Similar to Figure B7 for sol A/1959.

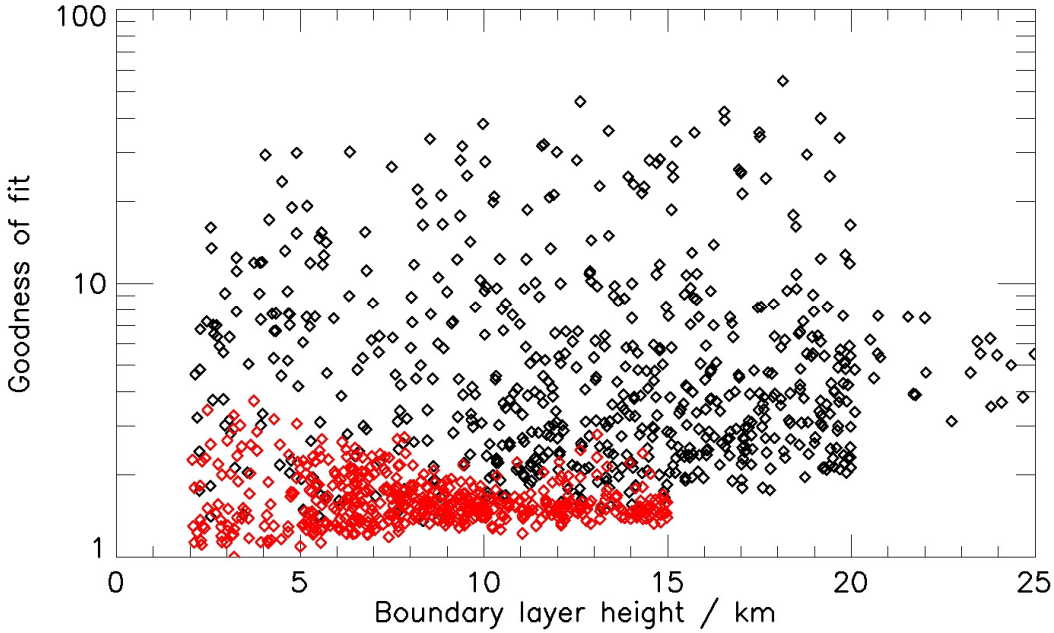

Figure B14. Similar to Figure B8 for sol A/1959.

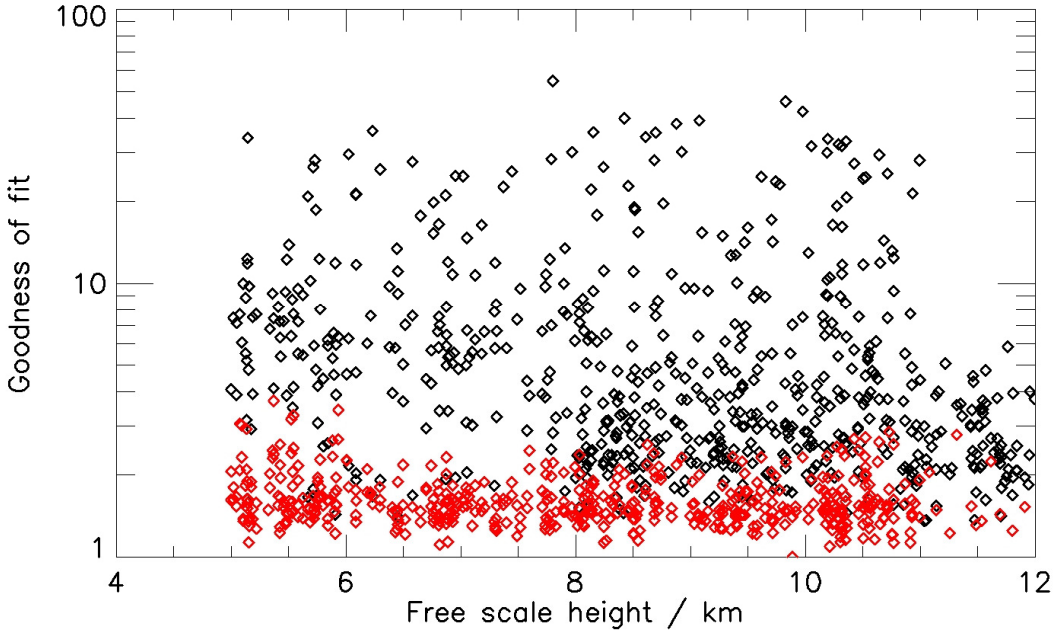

Figure B15. Similar to Figure B9 for sol A/1959.

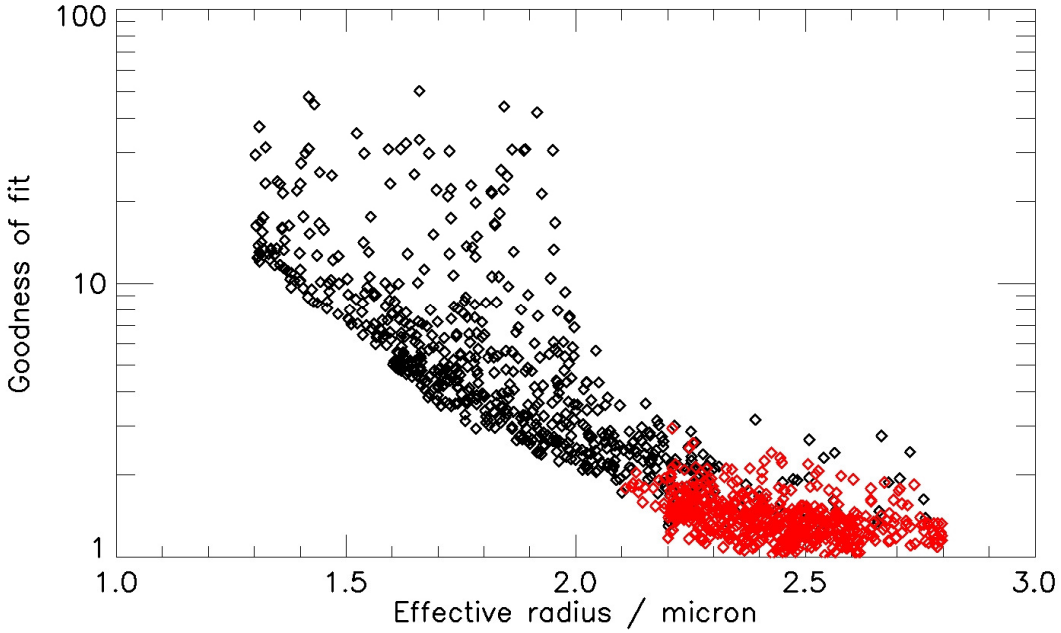

Figure B16. Similar to Figure B10 for sol A/1959.

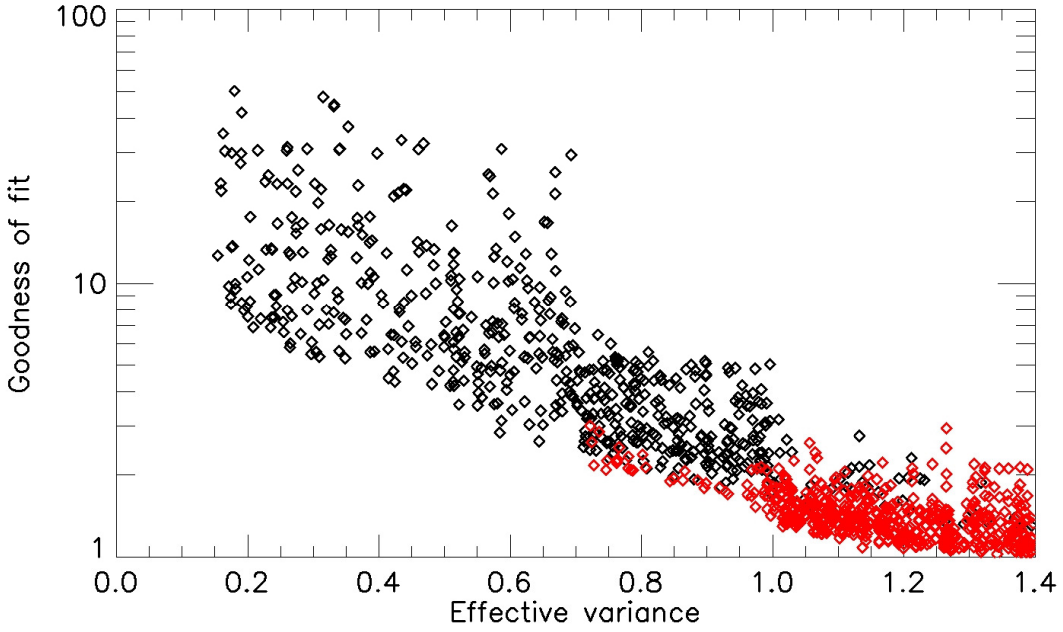

Figure B17. Similar to Figure B11 for sol A/1959.

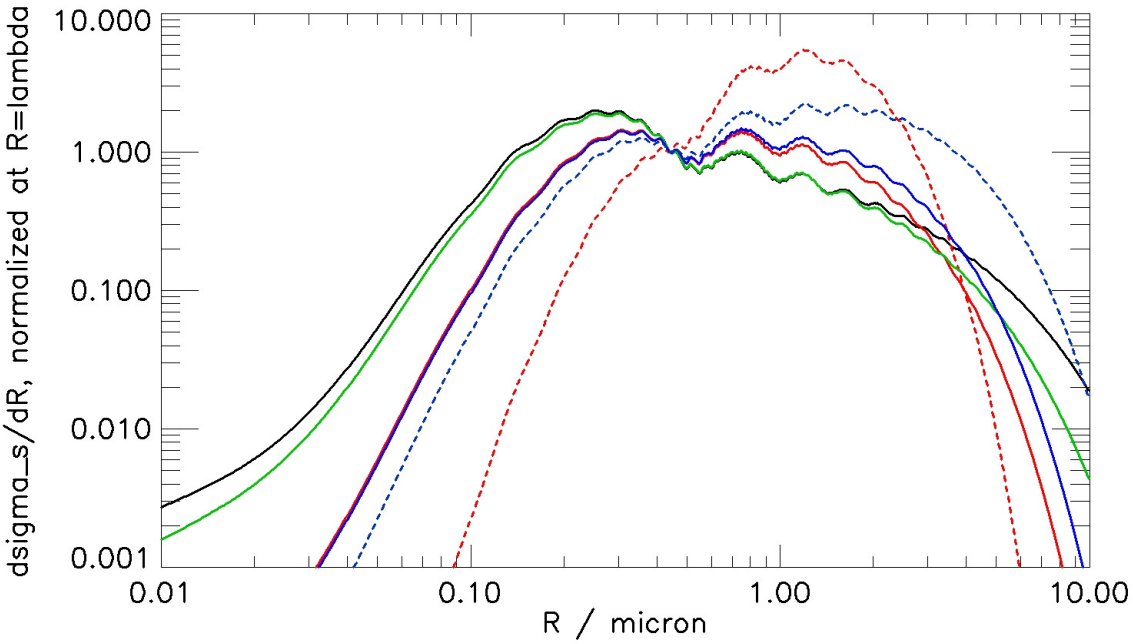

Figure B18. The curve is N(r) * Q * Π * r^2, normalized to 1 at r=lambda (.44 microns), where Q is extinction efficiency and N(r) is the Hansen-gamma size distribution function). Black: a=2.4, b=1.2, representative of this study; Red solid = Tomasko et al., 1999 (a=1.6, b=0.5); Red dash = Tomasko et al., 1999 (a=1.6, b=0.2); Green = Clancy et al., 1995; Blue solid = Pollack et al., 1995; Blue dash = Toon et al., 1977.

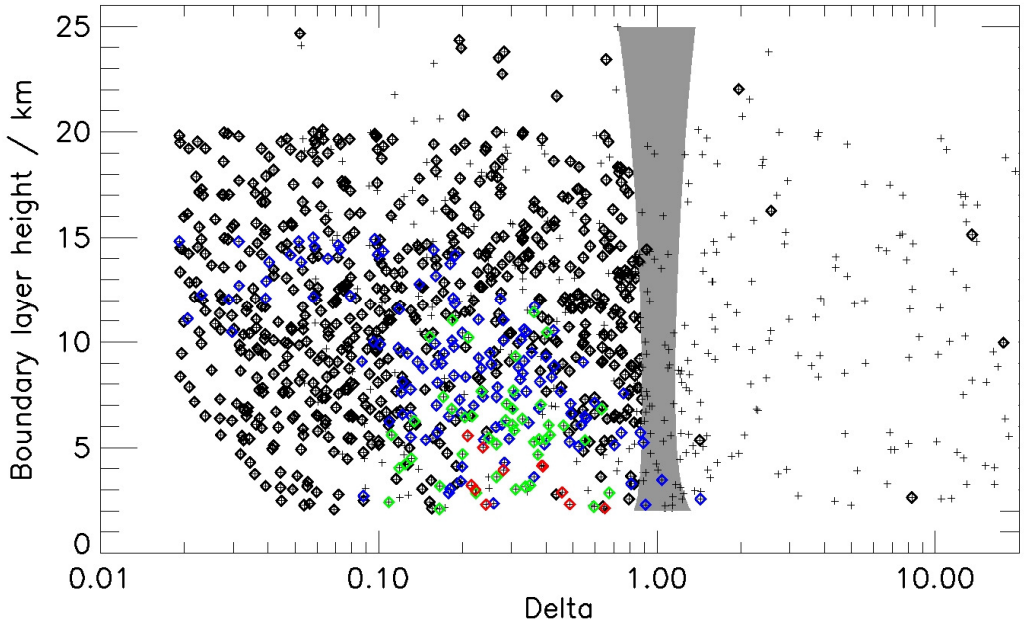

Figure B19. Similar to Figure B14 for sol A/1959.

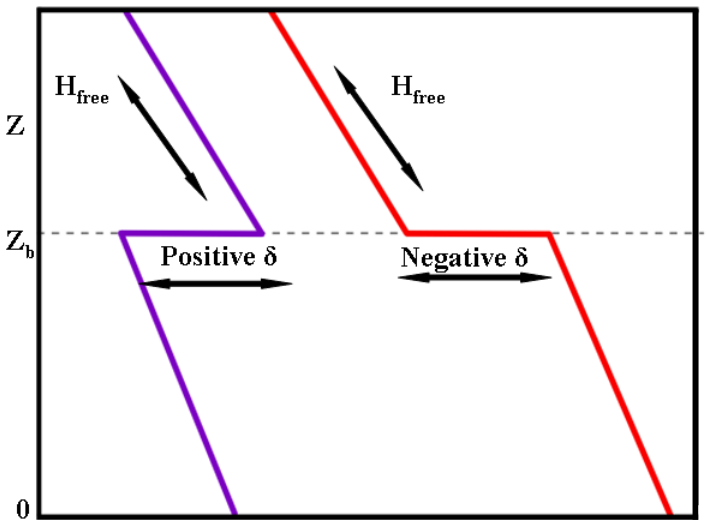

Figure B20. Schematic showing negative discontinuity for Spirit data and positive discontinuity for Opportunity data

VITA

Name:	Stephanie Beth Grounds
Address:	Texas A&M University, Atmospheric Sciences Department, Eller O&M Building – M/S 3150, College Station, TX. 77843-3150
Email Address:	sgroundstx@gmail.com
Education:	B.S., Physics, Minors in Mathematics and Chemistry, Angelo State University, 1994 M.S., Computer Information Systems, University of Phoenix, 2004